

See discussions, stats, and author profiles for this publication at: <https://www.researchgate.net/publication/268562522>

# Boomerang Flight Dynamics

Conference Paper · June 2012

DOI: 10.2514/6.2012-2650

---

CITATIONS

6

---

READS

3,918

1 author:



[J. Vassberg](#)

The Boeing Company Retired

94 PUBLICATIONS 3,437 CITATIONS

SEE PROFILE

Some of the authors of this publication are also working on these related projects:



DPW-VI Grids [View project](#)

## Boomerang Flight Dynamics

John C. Vassberg\*

*Long Beach, California 90803*

*Aerodynamics Lecture*

30<sup>th</sup> AIAA Applied Aerodynamics Conference  
New Orleans, Louisiana  
28 June, 2012



### Abstract

Aerodynamic characteristics and flight dynamics of boomerangs are investigated. A basic aerodynamic model, developed in the 1960's, is expanded upon using Blade Element Theory. The new aerodynamic model is coupled with a gyroscope model for rudimentary analyses. Some significant findings are made regarding the radius of a boomerang's circular flight path, the required inclination angle of its axis-of-rotation, its trim state, as well as its dynamic stability. These discoveries provide a basic understanding of how the interplay between aerodynamic forces and moments, and gyroscopic precession combine to return the boomerang to its rightful owner by way of a circular flight path.

A traditional V-shaped boomerang design is developed as a case study for further detailed analyses. Unsteady Reynolds-averaged Navier-Stokes solutions provide accurate aerodynamic characteristics of the subject boomerang. The high-fidelity aerodynamic model is coupled with the equations of motion to provide accurate six-degree-of-freedom simulations of boomerang flight dynamics. Boomerang orientation during its flight trajectory is described by the classical Euler angles.

---

\*Boeing Technical Fellow, Fellow AIAA, Boomerang Novice

# Nomenclature

$a, b, c, d$	Arbitrary Coefficients	$s$	Vector in Rotation Plane $\perp \mathbf{n}$
$\mathbf{b}$	Coordinate Vectors of Body Frame	$S$	Reference Area = $RC$
$C$	Blade Reference Chord	$T$	Transformation Matrix
$C_l$	2D Lift Coefficient = $\frac{Lift}{qC}$	$TE$	Airfoil Trailing Edge
$C_{l0}$	2D Lift Coefficient at $\alpha = 0$	$V$	Velocity
$C_{l\alpha}$	2D Lift-Curve Slope	$x$	Streamwise Cartesian Coordinate
$C_L$	3D Lift Coefficient = $\frac{Lift}{qS}$	$y$	Lateral Cartesian Coordinate
$C_M$	3D Rolling-Moment Coefficient	$z$	Vertical Cartesian Coordinate
$C_P$	Pressure Coefficient = $\frac{P-P_\infty}{q_\infty}$		
$g$	Gravitational Acceleration $\simeq 32 \frac{ft}{sec^2}$	$ND$	Non-Dimensionalized
$\mathbf{i}$	Coordinate Vectors of Inertial Frame	$2D$	Two Dimensional
$I$	Moment of Inertia	$3D$	Three Dimensional
$L$	Lift		
$L_0$	Basic Lift	$\alpha$	Angle-of-Attack
$L_\alpha$	Lift due to Angle-of-Attack	$\eta$	Fraction of Blade Radius = $\frac{r}{R}$
$LE$	Airfoil Leading Edge	$\theta$	Euler Angle: Orbital-Plane Inclination
$m$	Mass	$\pi$	3.141592654...
$M$	Rolling-Moment	$\rho$	Air Density = $1.3755 \times 10^{-6} \text{ slugs/in}^3$
$M_0$	Basic Rolling-Moment	$\phi$	Euler Angle: Right Ascension
$M_\alpha$	Rolling-Moment due to Angle-of-Attack	$\chi$	ND Rotational Velocity = $\frac{\omega R}{V}$
$\mathbf{n}$	Node Vector of Body Frame	$\hat{\chi}$	Lessor of $\chi$ or 1; = $\min(\chi, 1)$
$q$	Dynamic Pressure = $\frac{1}{2}\rho V^2$	$\psi$	Euler Angle: Argument of Perigee
$r$	Radial Coordinate	$\psi_c$	Cut-Off Angle = $\cos^{-1}(-\chi)$
$R$	Reference Radius of Blade	$\omega$	Rotational Velocity
$\mathcal{R}_p$	Radius of Circular Flight Path		

## I. Introduction

Boomerangs are deceptively simple-looking devices. But make no mistake, boomerang aerodynamics are rather complex. Not only is the flow unsteady and very three dimensional; it also reverses itself across the wing such that the leading and trailing edges swap roles twice every cycle. Furthermore, the Reynolds number is very low,  $\mathcal{O}(50,000)$ .

In spite of these challenges and by trial and error, Australian Aborigines managed to develop boomerang technology some 10,000 years ago; see Lorenz,<sup>1</sup> Mauro<sup>2</sup> and Hanson.<sup>3</sup> In fact, several civilizations developed straight-flying "boomerangs" for hunting and war many millenia ago. A gold-tip throwing-stick was found in King Tutankhamun's tomb. A boomerang was found in the sand dunes of The Netherlands that dates back 2,400 years. An exquisite mammoth-tusk throwing stick found in Poland is about 23,000 years old. This unique artifact has a mass of about 800 grams, a span of almost 70 cm, a chord of about 6 cm and is 1.5 cm thick. The ivory of this relic has a density of about 1,900 kg-per-cubic-meter. These ancient throwing sticks have aerodynamic and gyroscopic properties that stabilize their flights and extend their range. However, it was only the Aborigines who created the returning boomerang which they used primarily for recreation and sport, just as we do today. Indirectly, they also used the returning boomerang to aid in hunting fowl. Here, they would throw a boomerang over a flock of ducks floating on a pond. The waterfowl would mistake the boomerang for a hawk and would take flight, yet remain low to avoid the "predator". The low-flying game would then be well within range of hunters waiting nearby. Another unusual, but very utilitarian, use of the boomerang is when the Aborigines rubbed the leading edge against another piece of wood in a sawing motion to ignite a fire.

Figure 1 provides a small sampling of early 20<sup>th</sup>-century Aboriginal boomerangs. The boomerangs in this figure are probably straight-flying configurations. However, it is hard to know without throwing them - it is possible they are of the returning type. Figure 2 illustrates a wide variety of modern-day boomerangs; all of these examples are returning designs. Of particular note are the Tri-Fly and LED boomerangs, as these are utilized by the author for flight tests and further analysis in this body of work. The middle V-

type boomerang of the modern Aboriginal group is similar to a design developed herein for the purpose of high-fidelity analysis using computational fluid dynamics.

A number of boomerang world records as of June 2010 are included; see Wikipedia.<sup>4</sup> The most number of catches made within 5 minutes is 81 by Manuel Schutz, Switzerland, 2005. The quickest five-throw-catch sequence is 14.6 seconds by Adam Ruhf, USA, 1996. The most number of consecutive catches is 2,251 by Haruki Taketomi, Japan, 2009. The maximum time aloft in the unlimited class is 380.6 seconds by Billy Brazelton, USA, 2010. The farthest distance out for a returning flight is 238 meters by Manuel Schutz, Switzerland, 1999. The longest hand-held throw of any object was set in 2005 by David Schummy when he threw a boomerang 427.2 meters (over a quarter-mile). All of these are incredible statistics; little did the Aborigines know just how far their returning sticks could go.

This paper is organized in the following manner. Section II introduces Euler's classical orientation angles. Section III derives the equations of angular motion associated with boomerang dynamics. Section IV provides a discussion regarding the kinematics of an over-hand boomerang throw. Section V revisits work done in the 1960's regarding the aerodynamics of a boomerang. Section VI develops a new aerodynamic model for boomerangs based on blade element theory. Section VII develops general formulas for the radius of a boomerang's circular flight path, as well as the rotation-plane inclination angle. Section VIII develops a general condition for static trim and proves that dynamic stability is an intrinsic property of the boomerang. Section IX develops a traditional V-type boomerang design for further analysis. Section X provides the two-dimensional steady-state CFD results for the boomerang airfoil. Section XI discusses the three-dimensional unsteady CFD results for the boomerang subjected to a fixed cyclic motion. Section XII provides a full 6-DOF numerical simulation of a boomerang in flight. Section XIII is a summary of conclusions. Throughout the text, references are given as positive superscripts while footnotes are indicated by negative superscripts. Tables of data are embedded within the text while all figures are appended to the end of the paper.

## II. Euler's Classical Orientation Angles

The classical Euler angles  $\phi$ ,  $\theta$  and  $\psi$  are shown in Figure 3. Also depicted in Figure 3 are the inertial and body-fixed coordinate systems, labeled as  $(\mathbf{i}_1, \mathbf{i}_2, \mathbf{i}_3)$  and  $(\mathbf{b}_1, \mathbf{b}_2, \mathbf{b}_3)$ , respectively. In celestial mechanics, the angles  $(\phi, \theta, \psi)$  are used to specify the orientation of an orbit. They are known as the right ascension of the ascending node, the inclination of the orbital plane, and the argument of perigee, respectively. For the boomerang problem, as set-up herein, the axis of rotation is about the  $\mathbf{b}_3$  vector,  $\theta$  describes the bank angle that the plane of rotation makes with the horizon, while the precession rate of  $\mathbf{b}_3$  about  $\mathbf{i}_3$  is given by  $\dot{\phi}$ .

Transforming from the inertial frame to the body frame can be accomplished with three rotations in series. Pay attention to the order of rotations as this is crucial. First rotate by  $\phi$  about the  $\mathbf{i}_3$ -axis, then by  $\theta$  about the node vector  $\mathbf{n}$  and finally with a rotation of  $\psi$  about the  $\mathbf{b}_3$ -axis. The complete transformation from the inertial frame to the body frame using this three-rotation sequence can be described as

$$T^{ib} = R(\psi; \mathbf{b}_3) R(\theta; \mathbf{n}) R(\phi; \mathbf{i}_3). \quad (1)$$

Here,  $R(\alpha; \mathbf{v})$  represents an elementary rotation of angle  $\alpha$  about vector  $\mathbf{v}$ . This sequence of rotations is graphically illustrated by Figure 4. Completing the multiplication symbolized by Eqn (1), one obtains the transformation matrix

$$T^{ib} = \begin{bmatrix} c\phi c\psi - s\phi c\theta s\psi & s\phi c\psi + c\phi c\theta s\psi & s\theta s\psi \\ -c\phi s\psi - s\phi c\theta c\psi & -s\phi s\psi + c\phi c\theta c\psi & s\theta c\psi \\ s\phi s\theta & -c\phi s\theta & c\theta \end{bmatrix}. \quad (2)$$

Here,  $c$  indicates cosine and  $s$  indicates sine. Since Eqn (2) is a pure rotation, its inverse is just its transpose. Hence, to transform from the body frame to the inertial frame, one uses

$$T^{bi} = \begin{bmatrix} c\phi c\psi - s\phi c\theta s\psi & -c\phi s\psi - s\phi c\theta c\psi & s\phi s\theta \\ s\phi c\psi + c\phi c\theta s\psi & -s\phi s\psi + c\phi c\theta c\psi & -c\phi s\theta \\ s\theta s\psi & s\theta c\psi & c\theta \end{bmatrix}. \quad (3)$$

The next section discusses Euler's equations of angular motion.

### III. Euler's Equations of Angular Motion

In this section, we begin with the equations of angular motion as defined by Wiesel<sup>5</sup> and then adapt them for boomerang dynamics. We start the discussion with a very generalized form of Euler's equations of angular motion, then progress through a series of simplifications which retain only essential elements of the equations needed to describe a level circular flight path typical of a returning boomerang. Further simplifications regarding mass properties are introduced which appropriately continue to capture the low-frequency content of dynamic motion for boomerang flight. While this may filter or blur some of the high-frequency motion within a spin cycle, it greatly reduces the complexity of the ensuing derivations presented throughout this body of work.

For the boomerang problem, the principal-axis frame naturally aligns with an appropriate body-fixed coordinate system. This is fortuitous as the equations of angular motion are simplest when expressed in the principal-axis body frame because the off-diagonal terms of the moment-of-inertia matrix vanish. In the present work, the origin of the principal-axis frame coincides with the center-of-mass of the boomerang. When the Euler angles are zeroed, the body and inertial frames are aligned; see initial state of Figure 4. In this position, the  $Z$ -axis is the axis-of-rotation,  $Y$  is in the spanwise direction and  $X$  is streamwise. Here, the boomerang reference plane coincides with the  $X$ - $Y$  plane where  $Z = 0$ , the boomerang's centerline coincides with the  $X$ -axis, the right wing resides in the half-space where  $Y \geq 0$  and the boomerang upper-surface resides in the  $Z \geq 0$  half-space. For this system, Euler's equations of angular motion are given as:

$$\begin{aligned} M_1 &= I_{11} \dot{\omega}_1 + (I_{33} - I_{22}) \omega_2 \omega_3 \\ M_2 &= I_{22} \dot{\omega}_2 + (I_{11} - I_{33}) \omega_1 \omega_3 \\ M_3 &= I_{33} \dot{\omega}_3 + (I_{22} - I_{11}) \omega_1 \omega_2. \end{aligned} \quad (4)$$

Here, the  $\omega$ -vector describes the angular rates in the principal body-axis frame. These equations provide the time-rate-of-change of the  $\omega$ -vector, yet only constitute one half of the rotational equations of motion. Another set of equations is needed which link the angular rates of the body frame to the orientation angles of the body in the inertial frame. The remaining set of equations is given as:

$$\begin{aligned} \omega_1 &= \dot{\phi} \sin \theta \sin \psi + \dot{\theta} \cos \psi \\ \omega_2 &= \dot{\phi} \sin \theta \cos \psi - \dot{\theta} \sin \psi \\ \omega_3 &= \dot{\psi} + \dot{\phi} \cos \theta. \end{aligned} \quad (5)$$

These equations transform the  $\omega$ -vector given by Eqn (4) to provide the time-rate-of-change of the Euler angles  $(\phi, \theta, \psi)$ . In practice, these angular velocities are used to update the orientation angles  $(\phi, \theta, \psi)$  for the body as a function of time.

#### Axi-Symmetric Body

If the body is axi-symmetric about one of the principal axes, then further simplifications can be made to the equations of angular motion. So how can a boomerang be axi-symmetric? This question is best answered if one views the boomerang when it is spinning fast, rather than when statically displayed. Just as this motion blurs the visual of the boomerang to appear as a spinning disk, the moments of inertia can be time-averaged in the  $X$ - $Y$  plane. Although this simplification alters high-frequency content, it retains sufficient mass properties to accurately describe low-frequency boomerang dynamics.

For the purpose of this discussion, let's assume that the body is symmetric about the  $\mathbf{b}_3$ -axis and a rolling-moment exists purely about the  $\mathbf{n}$ -axis. Let's designate this torque about the nodal line as  $M_n$ . See Figure 3 to get familiar with this situation. Note that the  $\mathbf{n}$ -axis is perpendicular to the  $\mathbf{b}_3$ -axis and thus can be described as a linear combination of  $\mathbf{b}_1$  and  $\mathbf{b}_2$ .

$$\mathbf{n} = \cos \psi \mathbf{b}_1 - \sin \psi \mathbf{b}_2 \quad (6)$$

Also define an  $\mathbf{s}$ -axis which is perpendicular to both the  $\mathbf{n}$ -axis and the  $\mathbf{b}_3$ -axis.

$$\mathbf{s} = \sin \psi \mathbf{b}_1 + \cos \psi \mathbf{b}_2 \quad (7)$$

Note that the  $\mathbf{s}$ -axis is not shown in Figure 3.

Because of symmetry, let's define a moment of inertia ( $I_{rr}$ ) that is constant for any radial in the  $(\mathbf{n}, \mathbf{s})$  plane. Hence,

$$I_{rr} \equiv I_{11} = I_{22}. \quad (8)$$

Combining Eqns (4-8) gives:

$$\begin{aligned} M_n &= I_{rr} \ddot{\theta} + (I_{33} - I_{rr}) \dot{\phi}^2 \sin \theta \cos \theta + I_{33} \dot{\psi} \dot{\phi} \sin \theta \\ M_s &= I_{rr} \ddot{\phi} \sin \theta + 2 I_{rr} \dot{\theta} \dot{\phi} \cos \theta - I_{33} \dot{\theta} (\dot{\psi} + \dot{\phi} \cos \theta) \\ M_3 &= I_{33} \frac{d}{dt} (\dot{\psi} + \dot{\phi} \cos \theta). \end{aligned} \quad (9)$$

### Axi-Symmetric Disk

If an axi-symmetric body is also planar and homogeneous (i.e., a disk), then the principal moments of inertia are simply:

$$I_{33} = \frac{1}{2} m R^2 = 2 I_{rr}, \quad (10)$$

where  $m$  is the mass of the disk and  $R$  its radius. Now, the equations of angular motion reduced to:

$$\begin{aligned} M_n &= \frac{1}{4} m R^2 [\ddot{\theta} + \dot{\phi}^2 \sin \theta \cos \theta + 2 \dot{\psi} \dot{\phi} \sin \theta] \\ M_s &= \frac{1}{4} m R^2 [\ddot{\phi} \sin \theta - 2 \dot{\theta} \dot{\psi}] \\ M_3 &= \frac{1}{2} m R^2 \frac{d}{dt} [\dot{\psi} + \dot{\phi} \cos \theta]. \end{aligned} \quad (11)$$

For the moment, let's assume that the angular motion is such that  $\theta$  is constant, then  $\dot{\theta} = \ddot{\theta} = 0$ . Now, if the rolling-moment is purely about the  $\mathbf{n}$ -axis, then  $M_s = 0$ . Let's also assume that there is no moment being applied about the spin axis, i.e.,  $M_3 = 0$ . Under these conditions, the equations of angular motion reduce further to:

$$\begin{aligned} M_n &= \frac{1}{4} m R^2 [\dot{\phi}^2 \sin \theta \cos \theta + 2 \dot{\psi} \dot{\phi} \sin \theta] \\ 0 &= \ddot{\phi} \\ 0 &= \ddot{\psi}. \end{aligned} \quad (12)$$

One may recognize these equations as those that describe the motion of an inclined toy gyroscope, with its tip resting on a table. Here, the high spin rate of the gyroscope disk remains at a constant  $\dot{\psi}$ , with the gyroscope slowly rotating around its pivot-point-vertical-axis with a constant precession rate of  $\dot{\phi}$ , all the while, maintaining a constant inclination angle  $\theta$ . This precessional motion is driven by the moment  $M_n$  created by the gyroscope's weight, multiplied by the lateral off-set distance between the pivot point and the gyroscope's center-of-mass. For boomerang dynamics, the moment ( $M_n$ ) is supplied aerodynamically.

If  $M_n$ ,  $\theta$  and  $\dot{\psi}$  are known, then  $\dot{\phi}$  can be determined using the quadratic formula applied to Eqn (12).

$$\dot{\phi} = \frac{1}{\cos \theta} \left[ -\dot{\psi} \pm \sqrt{\dot{\psi}^2 + \frac{4 \cos \theta M_n}{\sin \theta m R^2}} \right]. \quad (13)$$

From experience, we know that the direction of the precession is the same as that of the disk spin. Hence, the positive branch of Eqn (13) is physically correct. Further, if  $\dot{\phi} \ll \dot{\psi}$ , then solution of Eqn (13) can be approximated by:

$$\dot{\phi} \doteq \frac{2 M_n}{\sin \theta m R^2 \dot{\psi}} = \frac{M_n}{\sin \theta I_{33} \dot{\psi}}, \quad (14)$$

where the second form is included for the more general case of constant  $\theta$  motion. Eqn (14) can be directly derived from Eqn (12) by dropping the  $\dot{\phi}^2$  term; the intermediate step of Eqn (13) is included as a formality.

Eqns (12-14) will be used to develop a simplified analysis of a boomerang's flight dynamics to determine the radius of its circular flight path as well as other pertinent relationships.

The next section reviews the kinematics of an over-hand boomerang throw.

## IV. Kinematics of a Boomerang Throw

A brief discussion regarding the kinematics of a boomerang throw is included in this section. The primary objective is to understand how the initial conditions of the boomerang's kinetics are somewhat predetermined by the kinematic motion of an over-hand throw.

Consider holding a basketball in the cup of your hand and throwing it under-handed as if bowling. The natural motion associated with this toss has the basketball rolling off the fingertips just as the ball is being released. This establishes both a forward velocity as well as a rotational velocity for the basketball. When the basketball makes contact with the ground, its spin rate will remain essentially unchanged. Hence, the natural kinematics of bowling a basketball creates an initial relationship between the ball's velocity and its spin rate.

$$\omega R \doteq V \quad (15)$$

Here,  $V$  is the translational velocity of the basketball,  $\omega$  is its rotational velocity and  $R$  its radius. While the relationship defined in Eqn (15) is only an approximate one and the person bowling the basketball can bias it one way or the other, it is quite difficult to violate it entirely.

Let's now consider a boomerang throw and draw similarities with the above example. To start, one holds a blade of the boomerang near its tip, grasping it in the palm of his hand. Because of the width of the hand, the center of this grasp is located around 85%-90% of the blade's radius. Traditionally, a V-type configuration is held by the lifting blade, with the dingle blade<sup>-1</sup> pointed forward at the far end of the boomerang. The boomerang throw proceeds in a manner analogous to throwing a small axe or a hatchet over-handed. The plane of rotation is nearly vertical, with only a slight lay-over angle. Hence, the axis of rotation is nearly horizontal. In terms of Euler's orientation angles, this corresponds to an initial inclination angle of the rotation plane in the range:

$$70^\circ \leq \theta_0 \leq 80^\circ. \quad (16)$$

Since the boomerang blade must be firmly held, it does not roll out of the hand as efficiently as does the finger-tip roll of the basketball. Hence, the relationship between the initial translational and rotational velocities is slightly different than before. In the case of the boomerang throw, we draw from experience, make an educated guess, and assume this relationship to be:

$$\omega_0 R \doteq 0.85 V_0. \quad (17)$$

Here,  $\omega_0$  and  $V_0$  are the boomerang's initial rotational and translational velocities, respectively. Also define the initial rotational velocity ( $\omega_0$ ) of Eqn (17) in a nondimensionalized form; this form will be used throughout the body of this work.

$$\chi_0 \equiv \frac{\omega_0 R}{V_0} \doteq 0.85 \quad (18)$$

The initial condition of Eqns (17-18) has the forward-going tip moving at  $1.85 V_0$  and the bottom tip also moving forward but only at a speed of  $0.15 V_0$ . In practice, a typical throw of a boomerang will yield a translational speed of about 60 *mph*, with a rotational cadence of about 10 *Hz*.

### Analysis of a Night Flight

In order to verify the assumption made by Eqns (17-18), we analyze a strobed image of a boomerang in night flight;<sup>6</sup> see Figures 5-6. In Figure 5, note the insert at the bottom-right corner. This insert shows a close-up view of a three-bladed boomerang with an LED strobe light located on each blade at 75% of its radius. Also in Figure 5 is a red rectangular box that traps a portion of the flight path approximately perpendicular to the camera's view. This segment of the flight path is depicted in Figure 6 and is further analyzed. Since there are three strobed paths, focus on the one centered about the solid bold vertical aqua line. To extract the relationship between translational and rotational velocities of the boomerang at this stage of its flight, a hypocycloid is fit through the strobed curve of interest. The result is shown as the bold gray line that fits the strobed-light path. The hypocycloid corresponding to this path is graphically given by the very-large-radius circular contact surface depicted by the orange line at the bottom of the image and the rolling wheel given by the yellow circle. The green circle in this figure represents the swept area of the boomerang while the gray circle coincides with the location of the LED light. Finally, the ratio of the

<sup>-1</sup>The dingle blade is the blade most-influenced by the wake of the other for a V-type boomerang.

radii of the gray-to-green circles provides a derived relationship of rotational-to-translational velocities for this flight segment. In this particular case, the initial condition of Eqns (17-18) is exactly verified. In the author's experience, the translational velocity decays slightly faster than does the rotational velocity during the course of a boomerang flight. Hence, the nondimensionalized rotational velocity ( $\chi$ ) of a boomerang increases during the course of its mission, from start to finish, so we have:

$$\frac{d\chi}{dt} > 0. \quad (19)$$

This property will be used in Section VII to explain why the inclination angle of a properly-design boomerang reduces during flight.

### Inducing a High-Spin-Rate Flight

Due to the natural kinematics of a boomerang throw, it is almost impossible to induce an extremely-high rotational velocity at point of launch. However, if one throws a boomerang slightly downward (like throwing a skipping stone) and bounces it off the ground, a high-spin-rate flight can be achieved. In essence, some of the translational kinetic energy gets impulsively converted to rotational kinetic energy. To establish a rough order-of-magnitude estimate, assume that the instantaneous bounce event conserves kinetic energy. Using the moment of inertia of a disk from Eqn (10), the states before and after the bounce are related as:

$$\begin{aligned} \frac{1}{2}m V_0^2 + \frac{1}{2}I \omega_0^2 &\doteq \frac{1}{2}m V_1^2 + \frac{1}{2}I \omega_1^2 \\ 2 V_0^2 + (\omega_0 R)^2 &\doteq 2 V_1^2 + (\omega_1 R)^2 \\ [2 + \chi_0^2] V_0^2 &\doteq [2 + \chi_1^2] V_1^2. \end{aligned} \quad (20)$$

where  $R$  is the radius of the boomerang, and subscripts 0 and 1 indicate the states before and after the bounce event, respectively. With some rearrangement, substitution of Eqn (17) into Eqn (20) gives:

$$\left(\frac{\omega_1}{\omega_0}\right)^2 \doteq \left[ \frac{2.7225 - 2 \left(\frac{V_1}{V_0}\right)^2}{0.7225} \right] \quad (21)$$

$$\left(\frac{\chi_1}{\chi_0}\right)^2 \doteq \left[ \frac{2.7225 \left(\frac{V_0}{V_1}\right)^2 - 2}{0.7225} \right]. \quad (22)$$

Hence, if the bounce event reduces the translational velocity ( $V$ ) by 50%, the rotational velocity ( $\omega$ ) will increase by about 75%. However in nondimensionalized terms, the ratio between rotational and translational velocities change by a factor of about 3.5 due to the impulse of the bounce, to give  $\chi_1 \doteq 3.0$ .

The next section provides some background on work done in the field of boomerang flight dynamics nearly 50 years ago.

## V. Felix Hess Model

In the 1960's, the aerodynamics of boomerangs was studied by Felix Hess.<sup>7</sup> Hess concluded that for sufficiently rapid rotation, the time-averaged lift and rolling-moment of an advancing boomerang are directly proportional to  $\omega^2$  and  $\omega V$ , respectively. Hence,

$$\bar{L} = a \omega^2 \quad , \quad \bar{M} = b \omega V, \quad (23)$$

where  $a$  and  $b$  are constants of proportionality,  $\omega$  is the rotational speed of the boomerang, and  $V$  is its flight speed. Note that the coefficients  $a$  and  $b$  lump together both aerodynamic characteristics and mass properties of a given boomerang. The units of  $a$  and  $b$  are  $lbs\text{-}sec^2$ .

Hess utilized his aerodynamic model, given by Eqn (23), in conjunction with the gyroscope model given by Eqn (11), to develop representative flight paths for a family of boomerangs, simply by varying the coefficients



$a$  and  $b$ . A deficiency of Hess' aerodynamics model is that it cannot self trim. Further, if manually trimmed, it is neutrally stable. However from practice, we know that boomerangs are dynamically stable over a wide variety of shapes and flight conditions; there must exist an inherent self-trimming capability in their designs. Hence, further work is needed to develop an aerodynamics model that can accommodate this characteristic.

For easier comparison later, Hess' model, given by Eqn (23), is reformulated. In the current work, the rotational speed ( $\omega$ ) is nondimensionalized as follows.

$$\chi = \frac{\omega R}{V} = \frac{V_{tip}}{V}, \quad (24)$$

where  $R$  is the radius of boomerang blades, and  $V_{tip}$  is the blade tip speed due to rotation. We also refer to  $\chi$  as the tip-speed ratio. Substitution of Eqn (24) into Eqn (23) gives Hess' aerodynamic model in terms of  $\chi$  as:

$$\bar{L} = \left( \frac{a}{R^2} \right) \chi^2 V^2 \quad , \quad \bar{M} = \left( \frac{b}{R} \right) \chi V^2, \quad (25)$$

where the bracketed terms are now the constants of proportionality.

Time-averaged relationships for lift and rolling-moment will be significantly enhanced in the next section using Blade Element Theory.

## VI. Blade Element Theory

An aerodynamic model is developed herein using Blade Element Theory (BET). This model uses the lift-curve of a boomerang's two-dimensional airfoil section and it is assumed that the boomerang operates at angles-of-attack close to zero.<sup>-2</sup> Hence, the relationship between lift and alpha is essentially linear.

$$C_l(\alpha) = C_{l0} + \alpha C_{l\alpha}. \quad (26)$$

Here,  $\alpha$  is the angle-of-attack of the airfoil,  $C_{l0}$  is its lift coefficient at  $\alpha = 0$  and  $C_{l\alpha}$  is the slope of the lift curve. These values will be determined numerically by running computational fluid dynamics (CFD) on a representative airfoil section of the boomerang blade over a range of angles-of-attack.

Figure 7 provides a top-view schematic of a single, non-tapered blade that rotates about the  $Z$ -axis in a counter-clockwise manner. In this figure,  $R$  is the radius of the blade,  $C$  is its chord and the freestream velocity ( $V$ ) is aligned with the  $X$ -axis. Also in this schematic,  $\psi$  is the angular position of the blade, where  $\psi = 0$  represents the position when the advancing blade is perpendicular to the freestream flow.  $V_n$  is the local normal on-set velocity component to a blade section; it is a function of radial and angular positions and is given by:

$$V_n(r, \psi) = V \cos \psi + \omega r. \quad (27)$$

Here,  $\omega = \dot{\psi}$  is the rotational speed of the blade spinning about the  $Z$ -axis. In the present work, this rotational speed is nondimensionalized as follows.

$$\chi = \frac{\omega R}{V}. \quad (28)$$

Figures 8-10 illustrate how  $V_n$  varies within the disk area swept by the blade for rotational speeds of  $\chi = (0.7, 1.0, 1.5)$ , respectively. In these images, the freestream velocity is from left-to-right. Note that  $V_n < 0$  is depicted by the blue-shaded regions which only occur when  $90^\circ \leq \psi \leq 270^\circ$ . As an aside, the  $V_n = 0$  contour is a circle of diameter  $\frac{1}{\chi}$ .

In general, the rotational plane of the blade can be at an angle-of-attack ( $\alpha$ ) to the freestream velocity ( $V$ ). The velocity component normal to the rotational plane ( $V_z$ ) can be approximated as:

$$V_z = V \sin \alpha \doteq \alpha V \quad , \quad |\alpha| \ll 1. \quad (29)$$

As the blade sweeps in  $\psi$ , the airfoil sections along its span are subjected to a cyclic variation of both normal velocity ( $V_n$ ) and apparent angle-of-attack. Designate this effective angle-of-attack as  $\alpha_n$  and approximate with:

$$\alpha_n = \tan^{-1} \left( \frac{V_z}{|V_n|} \right) \doteq \frac{V_z}{|V_n|} \quad , \quad |V_z| \ll |V_n|. \quad (30)$$

---

<sup>-2</sup>Actually, very large angles-of-attack exist, but only at very low dynamic pressures, so the error introduced is minimal.

The reason the absolute value of  $V_n$  is needed above is because, even when  $V_n$  is negative, the sign of lift due to angle-of-attack is solely determined by the sign of  $V_z$ . As will be seen later, this complicates matters in the derivations for lift and rolling-moment due to angle-of-attack.

While all boomerangs have more than one blade, with blade element theory each are treated identically; there is no distinction between the force and moments of the lifting and dingle blades. As a consequence, deriving the coefficients of lift and rolling-moment for a single blade is equivalent to doing so for an  $N$ -bladed configuration. For example, a 3-bladed boomerang will have 3 times the lift of one of its blades but its lift will also be nondimensionalized by 3 times the reference area of a blade.

## Lift Derivation

The next step is to develop a relationship for the dimensional lift generated by the blade as a function of its angular position ( $\psi$ ).

$$\begin{aligned}
 L(\psi) &= \int_0^R \frac{1}{2} \rho V_n^2 C_l(\alpha_n) C dr \\
 &= \frac{1}{2} \rho C \int_0^R V_n^2 \left[ C_{l0} + \frac{V_z}{|V_n|} C_{l\alpha} \right] dr \\
 &= \frac{1}{2} \rho C \int_0^R [V_n^2 C_{l0} + |V_n| V_z C_{l\alpha}] dr.
 \end{aligned} \tag{31}$$

Here, the integration is over the span of the blade,  $\rho$  is air density,  $C_l(\alpha_n)$  is the 2D sectional lift coefficient given by Eqn (26), but now as a function of  $\alpha_n$  and  $C$  is chord length. Eqns (26-30) have also been incorporated into Eqn (31). By observation, note that the total lift of Eqn (31) can be split into a basic lift and a lift due to angle-of-attack. To help keep the remaining derivations manageable, we will develop these lifts separately, then combine later.

### Basic Lift

In the context of this work, basic lift is defined as that which is generated by an airfoil acting at no angle-of-attack to its onset flow. Starting with the first term of the integrand of Eqn (31), and substituting Eqns (27-28), the basic-lift derivation continues as:

$$\begin{aligned}
 L_0(\psi) &= \frac{1}{2} \rho C C_{l0} \int_0^R [V \cos \psi + \omega r]^2 dr \\
 &= \frac{1}{2} \rho V^2 C C_{l0} \int_0^R \cos^2 \psi + 2 \cos \psi \chi \left( \frac{r}{R} \right) + \chi^2 \left( \frac{r}{R} \right)^2 dr \\
 &= \frac{1}{2} \rho V^2 R C C_{l0} \left[ \cos^2 \psi + \cos \psi \chi + \frac{1}{3} \chi^2 \right]_0^R \\
 &= q S C_{l0} \left[ \cos^2 \psi + \cos \psi \chi + \frac{1}{3} \chi^2 \right].
 \end{aligned} \tag{32}$$

where  $q = \frac{1}{2} \rho V^2$  is the freestream dynamic pressure and  $S = RC$  is the blade planform area.

To determine a time-averaged value for the basic lift,  $L_0(\psi)$  is integrated over  $\psi$ . However, since  $L_0$  is symmetric about the  $Y$ -axis, this integration can be performed from 0 to  $\pi$ .

$$\begin{aligned}
 \bar{L}_0 &= \frac{1}{\pi} \int_0^\pi L_0(\psi) d\psi \\
 &= \frac{1}{\pi} q S C_{l0} \left[ \frac{1}{2} (\psi + \sin \psi \cos \psi) + \chi \sin \psi + \frac{1}{3} \chi^2 \psi \right]_0^\pi \\
 &= q S C_{l0} \left[ \frac{1}{2} + \frac{1}{3} \chi^2 \right]
 \end{aligned} \tag{33}$$

Comparing Eqn (33) with Eqn (25) illustrates that Hess' aerodynamic model is insufficient for small rotational speeds where  $\chi < 1.5$ , even for basic lift.

### Special Integration Topic

Before proceeding to the derivation of the lift due to angle-of-attack, it will be necessary to briefly touch on a special integration topic. Consider a line segment on the interval  $[0, 1]$  of the form  $y(x) = a + bx$ . If this segment is either completely above or below the  $X$ -axis, then an integration of its absolute value is trivial. However, let's consider the situation where the line starts below the  $X$ -axis at  $x = 0$  and ends above it at  $x = 1$ . For this case, it can be shown that:

$$\int_0^1 |a + bx| dx = \left[ \frac{a^2}{b} + a + \frac{b}{2} \right] \quad , \quad a \leq 0 \leq |a| \leq b. \quad (34)$$

Here,  $a$  and  $b$  are arbitrary constants. Note that the first term in the square brackets of Eqn (34) is an addition to the result one would get if the integrand had not been made an absolute value.

### Lift due to Angle-of-Attack

We now proceed with the derivation of lift due to angle-of-attack, starting with the second term of the integrand of Eqn (31).

$$\begin{aligned} L_\alpha(\psi) &= \frac{1}{2} \rho C \int_0^R |V_n| V_z C_{l\alpha} dr \\ &= \frac{1}{2} \rho C \int_0^R |V \cos \psi + \omega r| \alpha V C_{l\alpha} dr \\ &= \frac{1}{2} \rho V^2 \alpha C_{l\alpha} C \int_0^R \left| \cos \psi + \chi \left( \frac{r}{R} \right) \right| dr \\ &= q S \alpha C_{l\alpha} \int_0^1 |\cos \psi + \chi \eta| d\eta \end{aligned} \quad (35)$$

Here,  $\eta = \frac{r}{R}$  is the nondimensional spanwise coordinate along the blade. Because of the absolute-valued term inside the integral of Eqn (35), the following four cases exist for  $0 \leq \psi \leq \pi$ .

For  $0 \leq \psi \leq \frac{\pi}{2}$ , and any value of  $\chi > 0$ , the term  $[\cos \psi + \chi \eta] \geq 0$  over the interval of integration, so:

$$L_\alpha(\psi) = q S \alpha C_{l\alpha} \left[ \cos \psi + \frac{\chi}{2} \right]. \quad (36)$$

For  $\frac{\pi}{2} < \psi \leq \pi$ , and  $\chi \geq 1$ , the term  $[\cos \psi + \chi \eta]$  switches sign, so we apply Eqn (34) to get:

$$L_\alpha(\psi) = q S \alpha C_{l\alpha} \left[ \frac{\cos^2 \psi}{\chi} + \cos \psi + \frac{\chi}{2} \right]. \quad (37)$$

For  $\frac{\pi}{2} < \psi \leq \cos^{-1}(-\chi)$ , and  $\chi < 1$ , the term  $[\cos \psi + \chi \eta]$  also switches sign, and again we have:

$$L_\alpha(\psi) = q S \alpha C_{l\alpha} \left[ \frac{\cos^2 \psi}{\chi} + \cos \psi + \frac{\chi}{2} \right]. \quad (38)$$

For  $\cos^{-1}(-\chi) < \psi \leq \pi$ , and  $\chi < 1$ , the term  $[\cos \psi + \chi \eta] < 0$  over the interval, so:

$$L_\alpha(\psi) = q S \alpha C_{l\alpha} \left[ -\cos \psi - \frac{\chi}{2} \right]. \quad (39)$$

In order to determine a time-averaged value for lift due to angle-of-attack,  $L_\alpha(\psi)$  is integrated over  $\psi$  from 0 to  $\pi$ . It is possible to do this considering only two cases; one with  $\chi \geq 1$  and the other with  $\chi < 1$ . However, this does require a little manipulation of Eqns (36-39) when folded into the integration over  $\psi$ .

For  $\chi \geq 1$ ,

$$\begin{aligned} \bar{L}_\alpha &= \frac{1}{\pi} q S \alpha C_{l\alpha} \left\{ \int_0^\pi \left[ \cos \psi + \frac{\chi}{2} \right] d\psi + \int_{\frac{\pi}{2}}^\pi \left[ \frac{\cos^2 \psi}{\chi} \right] d\psi \right\} \\ &= \frac{1}{\pi} q S \alpha C_{l\alpha} \left\{ \left[ \sin \psi + \frac{\chi \psi}{2} \right]_0^\pi + \left[ \frac{1}{2\chi} (\psi + \sin \psi \cos \psi) \right]_{\frac{\pi}{2}}^\pi \right\} \\ &= q S \alpha C_{l\alpha} \left[ \frac{\chi}{2} + \frac{1}{4\chi} \right]. \end{aligned} \quad (40)$$

For  $\chi < 1$ ,

$$\begin{aligned}
\bar{L}_\alpha &= \frac{1}{\pi} q S \alpha C_{l\alpha} \left\{ \int_0^{\psi_c} \left[ \cos \psi + \frac{\chi}{2} \right] d\psi + \int_{\frac{\pi}{2}}^{\psi_c} \left[ \frac{\cos^2 \psi}{\chi} \right] d\psi - \int_{\psi_c}^{\pi} \left[ \cos \psi + \frac{\chi}{2} \right] d\psi \right\} \\
&= \frac{1}{\pi} q S \alpha C_{l\alpha} \left\{ \left[ \sin \psi + \frac{\chi \psi}{2} \right]_0^{\psi_c} + \left[ \frac{1}{2\chi} (\psi + \sin \psi \cos \psi) \right]_{\frac{\pi}{2}}^{\psi_c} - \left[ \sin \psi + \frac{\chi \psi}{2} \right]_{\psi_c}^{\pi} \right\} \\
&= \frac{1}{\pi} q S \alpha C_{l\alpha} \left\{ \frac{3}{2} \sqrt{1-\chi^2} + \chi \left[ \psi_c - \frac{\pi}{2} \right] + \frac{1}{2\chi} \left[ \psi_c - \frac{\pi}{2} \right] \right\} \\
&= \frac{1}{\pi} q S \alpha C_{l\alpha} \left\{ \frac{3}{2} \sqrt{1-\chi^2} + \left[ \chi + \frac{1}{2\chi} \right] \left[ \psi_c - \frac{\pi}{2} \right] \right\}. \tag{41}
\end{aligned}$$

where  $\psi_c = \cos^{-1}(-\chi)$ .

As it turns out, boomerangs require a spin rate sufficient to be stable in flight. Furthermore, the kinematics of a boomerang throw naturally place the spin rate such that  $\chi = \mathcal{O}(1)$ . Depending on the person, this typically results in spin rates of  $\chi \geq 0.7$ . With a lower limit on  $\chi$  being known, let's expand the arc-cosine about  $\chi_0 = 1$  as follows.

$$\psi_c = \cos^{-1}(-\chi) \doteq \left[ \pi - 2\sqrt{1-\chi} \right] - \frac{1}{6\sqrt{2}}(1-\chi)^{\frac{3}{2}} - \dots \tag{42}$$

Retaining only the bracketed two terms of this expansion is sufficient for our purposes and plugging these into Eqn (41) gives an approximate form that is more analogous with that of Eqn (40).

For  $0.7 < \chi < 1$ ,

$$\bar{L}_\alpha \doteq q S \alpha C_{l\alpha} \left\{ \left[ \frac{\chi}{2} + \frac{1}{4\chi} \right] \left[ 1 - \frac{2\sqrt{2}}{\pi} \sqrt{1-\chi} \right] + \frac{3}{2\pi} \sqrt{1-\chi^2} \right\}. \tag{43}$$

By observation, Eqns (40 & 43) exhibit a smooth transition across  $\chi = 1$  for the lift due to angle-of-attack; this is expected and serves as a sanity check that the derivation for lift due to angle-of-attack may be correct.

### Coefficient of Total Lift

Combining Eqns (33, 40, 43), gives an expression for total lift, and nondimensionalizing by  $(qS)$  provides a time-averaged total-lift coefficient for a boomerang based on blade element theory of:

$$\bar{C}_L = C_{l0} \left[ \frac{1}{2} + \frac{1}{3} \chi^2 \right] + \alpha C_{l\alpha} \left\{ \left[ \frac{\chi}{2} + \frac{1}{4\chi} \right] \left[ 1 - \frac{2\sqrt{2}}{\pi} \sqrt{1-\hat{\chi}} \right] + \frac{3}{2\pi} \sqrt{1-\hat{\chi}^2} \right\}, \tag{44}$$

where  $\hat{\chi} = \min(\chi, 1)$  and Eqn (44) is appropriate for  $\chi \geq 0.7$ .

### Rolling-Moment Derivation

The next step is to develop a relationship for the dimensional rolling-moment about the  $X$ -axis generated by the blade as a function of its angular position  $(\psi)$ .

$$\begin{aligned}
M(\psi) &= \int_0^R \frac{1}{2} \rho V_n^2 C_l(\alpha_n) C r \cos \psi dr \\
&= \frac{1}{2} \rho C \int_0^R V_n^2 \left[ C_{l0} + \frac{V_z}{|V_n|} C_{l\alpha} \right] r \cos \psi dr \\
&= \frac{1}{2} \rho C \int_0^R [V_n^2 C_{l0} + |V_n| V_z C_{l\alpha}] r \cos \psi dr. \tag{45}
\end{aligned}$$

Here, the integration is over the span of the blade,  $\rho$  is air density,  $C_l(\alpha_n)$  is the 2D sectional lift coefficient given by Eqn (26) and  $r \cos \psi$  is the  $y$ -arm on which a sectional lift acts to generate an incremental rolling-moment. Eqns (26-30) have been incorporated into Eqn (45). By observation, note that the total rolling-moment of Eqn (45) can be split into a moment due to basic lift and one due to angle-of-attack. To help keep the remaining derivations manageable, we will develop these rolling-moments separately, then combine later.

### Basic Rolling-Moment

In the context of this work, basic rolling-moment is defined as that which is generated by an airfoil acting at no angle-of-attack to its onset flow. Starting with the first term of the integrand of Eqn (45) and substituting Eqns (27-28), the derivation for the basic rolling-moment continues as:

$$\begin{aligned}
 M_0(\psi) &= \frac{1}{2} \rho C C_{l0} \int_0^R [V \cos \psi + \omega r]^2 r \cos \psi dr \\
 &= \frac{1}{2} \rho V^2 R C C_{l0} \int_0^R \cos^3 \psi \left( \frac{r}{R} \right) + 2 \cos^2 \psi \chi \left( \frac{r}{R} \right)^2 + \chi^2 \left( \frac{r}{R} \right)^3 \cos \psi dr \\
 &= q S R C_{l0} \int_0^1 \cos^3 \psi \eta + 2 \cos^2 \psi \chi \eta^2 + \chi^2 \eta^3 \cos \psi d\eta \\
 &= q S R C_{l0} \left[ \frac{1}{2} \cos^3 \psi + \frac{2}{3} \cos^2 \psi \chi + \frac{1}{4} \cos \psi \chi^2 \right], \tag{46}
 \end{aligned}$$

where  $q = \frac{1}{2} \rho V^2$  is the freestream dynamic pressure,  $\eta = \frac{r}{R}$  is the nondimensional span along the blade,  $dr = R d\eta$  and  $S = R C$  is the blade planform area.

To determine a time-averaged value for the basic rolling-moment,  $M_0(\psi)$  is integrated over  $\psi$ . However, since  $M_0$  is symmetric about the  $Y$ -axis, this integration can be performed from 0 to  $\pi$ .

$$\begin{aligned}
 \bar{M}_0 &= \frac{1}{\pi} \int_0^\pi M_0(\psi) d\psi \\
 &= \frac{1}{\pi} q S R C_{l0} \left[ \frac{1}{24} (9 \sin \psi + \sin 3\psi) + \frac{1}{3} \chi (\psi + \sin \psi \cos \psi) + \frac{1}{4} \chi^2 \sin \psi \right]_0^\pi \\
 &= \frac{1}{3} q S R C_{l0} \chi. \tag{47}
 \end{aligned}$$

Comparing Eqn (47) with Eqn (25) illustrates that Hess' aerodynamic model for a time-averaged rolling-moment is analogous to the basic rolling-moment derived by blade element theory.

### Another Special Integration Topic

Before proceeding to the derivation of the rolling-moment due to angle-of-attack, it will be necessary to briefly touch on another special integration topic. Consider a parabola on the interval  $[0, 1]$  of the form  $y(x) = ax + bx^2$ . If this curve segment is either completely above or below the  $X$ -axis, then an integration of its absolute value is trivial. However, let's consider the situation where the curve moves below the  $X$ -axis at  $x = 0$  and ends up above it at  $x = 1$ . For this case, it can be shown that:

$$\int_0^1 |ax + bx^2| dx = \left[ \frac{-a^3}{3b^2} + \frac{a}{2} + \frac{b}{3} \right], \quad a \leq 0 \leq |a| \leq b. \tag{48}$$

Here,  $a$  and  $b$  are arbitrary constants. Note that the first term in the square brackets of Eqn (48) is a positive value and is an addition to the result one would get if the integrand had not been made an absolute value.

### Rolling-Moment due to Angle-of-Attack

We now continue with the derivation of rolling-moment due to angle-of-attack, starting with the second term of the integrand of Eqn (45).

$$\begin{aligned}
 M_\alpha(\psi) &= \frac{1}{2} \rho C \int_0^R |V_n| V_z r \cos \psi C_{l\alpha} dr \\
 &= \frac{1}{2} \rho C \int_0^R |V \cos \psi + \omega r| \alpha V r \cos \psi C_{l\alpha} dr \\
 &= \frac{1}{2} \rho V^2 \alpha C_{l\alpha} C \int_0^R \left| \cos \psi + \chi \left( \frac{r}{R} \right) \right| r \cos \psi dr \\
 &= q S \alpha C_{l\alpha} \cos \psi \int_0^1 |\cos \psi + \chi \eta| \eta d\eta. \tag{49}
 \end{aligned}$$

Here,  $\eta = \frac{r}{R}$  is the nondimensional spanwise coordinate along the blade. Because of the absolute-valued term inside the integral of Eqn (49), the following four cases exist for  $0 \leq \psi \leq \pi$ .

For  $0 \leq \psi \leq \frac{\pi}{2}$ , and any value of  $\chi > 0$ , the term  $[\cos \psi + \chi \eta] \geq 0$  over the interval of integration, so:

$$M_\alpha(\psi) = q S R \alpha C_{l\alpha} \left[ \frac{1}{2} \cos^2 \psi + \frac{\chi}{3} \cos \psi \right]. \quad (50)$$

For  $\frac{\pi}{2} < \psi \leq \pi$ , and  $\chi \geq 1$ , the term  $[\cos \psi + \chi \eta]$  switches sign, so we apply Eqn (48) to get:

$$M_\alpha(\psi) = q S R \alpha C_{l\alpha} \left[ \frac{-\cos^4 \psi}{3 \chi^2} + \frac{1}{2} \cos^2 \psi + \frac{\chi}{3} \cos \psi \right]. \quad (51)$$

For  $\frac{\pi}{2} < \psi \leq \cos^{-1}(-\chi)$ , and  $\chi < 1$ , the term  $[\cos \psi + \chi \eta]$  also switches sign, and again we have:

$$M_\alpha(\psi) = q S R \alpha C_{l\alpha} \left[ \frac{-\cos^4 \psi}{3 \chi^2} + \frac{1}{2} \cos^2 \psi + \frac{\chi}{3} \cos \psi \right]. \quad (52)$$

For  $\cos^{-1}(-\chi) < \psi \leq \pi$ , and  $\chi < 1$ , the term  $[\cos \psi + \chi \eta] < 0$  over the interval, so:

$$M_\alpha(\psi) = q S R \alpha C_{l\alpha} \left[ -\frac{1}{2} \cos^2 \psi - \frac{\chi}{3} \cos \psi \right]. \quad (53)$$

To determine a time-averaged value for rolling-moment due to angle-of-attack,  $M_\alpha(\psi)$  is integrated over  $\psi$  from 0 to  $\pi$ . It is possible to do this considering only two cases; one with  $\chi \geq 1$  and the other with  $\chi < 1$ . However, this does require a little manipulation of Eqns (50-53) when folded into the integration over  $\psi$ .

For  $\chi \geq 1$ ,

$$\begin{aligned} \bar{M}_\alpha &= \frac{1}{\pi} q S R \alpha C_{l\alpha} \left\{ \int_0^\pi \left[ \frac{1}{2} \cos^2 \psi + \frac{\chi}{3} \cos \psi \right] d\psi + \int_{\frac{\pi}{2}}^\pi \left[ \frac{-\cos^4 \psi}{3 \chi^2} \right] d\psi \right\} \\ &= \frac{1}{\pi} q S R \alpha C_{l\alpha} \left\{ \left[ \frac{1}{4} (\psi + \sin \psi \cos \psi) + \frac{\chi}{3} \sin \psi \right]_0^\pi - \left[ \frac{12 \psi + 8 \sin 2 \psi + \sin 4 \psi}{96 \chi^2} \right]_{\frac{\pi}{2}}^\pi \right\} \\ &= q S R \alpha C_{l\alpha} \left[ \frac{1}{4} - \frac{1}{16 \chi^2} \right]. \end{aligned} \quad (54)$$

For  $\chi < 1$ ,

$$\begin{aligned} \bar{M}_\alpha &= \frac{1}{\pi} q S R \alpha C_{l\alpha} \left\{ \int_0^{\psi_c} \left[ \frac{1}{2} \cos^2 \psi + \frac{\chi}{3} \cos \psi \right] d\psi + \int_{\frac{\pi}{2}}^{\psi_c} \left[ \frac{-\cos^4 \psi}{3 \chi^2} \right] d\psi - \int_{\psi_c}^\pi \left[ \frac{1}{2} \cos^2 \psi + \frac{\chi}{3} \cos \psi \right] d\psi \right\} \\ &= \frac{1}{\pi} q S R \alpha C_{l\alpha} \left\{ \left[ \frac{\psi + \sin \psi \cos \psi}{4} + \frac{\chi}{3} \sin \psi \right]_{0, \pi}^{\psi_c} - \left[ \frac{12 \psi + 8 \sin 2 \psi + \sin 4 \psi}{96 \chi^2} \right]_{\frac{\pi}{2}}^{\psi_c} \right\} \\ &= \frac{1}{\pi} q S R \alpha C_{l\alpha} \left\{ \left[ \frac{\psi_c - \frac{\pi}{2} + \sin \psi_c \cos \psi_c}{2} + \frac{2 \chi}{3} \sin \psi_c \right] - \left[ \frac{12 \psi_c - 6 \pi + 8 \sin 2 \psi_c + \sin 4 \psi_c}{96 \chi^2} \right] \right\} \\ &= \frac{1}{\pi} q S R \alpha C_{l\alpha} \left\{ \frac{\psi_c - \chi \sqrt{1 - \chi^2}}{2} + \frac{2 \chi}{3} \sqrt{1 - \chi^2} - \frac{\pi}{4} - \frac{12 \psi_c - 6 \pi - (8 \chi^3 + 12 \chi) \sqrt{1 - \chi^2}}{96 \chi^2} \right\} \\ &= q S R \alpha C_{l\alpha} \left\{ \frac{1}{16 \chi^2} - \frac{\psi_c}{8 \pi \chi^2} + \frac{\sqrt{1 - \chi^2}}{8 \pi \chi} - \frac{1}{4} + \frac{\psi_c}{2 \pi} + \frac{\chi \sqrt{1 - \chi^2}}{4 \pi} \right\} \\ &= q S R \alpha C_{l\alpha} \left\{ \frac{(\pi - 2 \psi_c)}{16 \pi \chi^2} + \frac{\sqrt{1 - \chi^2}}{8 \pi \chi} - \frac{(\pi - 2 \psi_c)}{4 \pi} + \frac{\chi \sqrt{1 - \chi^2}}{4 \pi} \right\}. \end{aligned} \quad (55)$$

where  $\psi_c = \cos^{-1}(-\chi)$ . Note the nomenclature above:  $[\star]_{0, \pi}^{\chi_c} \equiv ([\star]_0^{\chi_c} + [\star]_{\pi}^{\chi_c}) \equiv ([\star]_0^{\chi_c} - [\star]_{\chi_c}^{\pi})$ .

Substituting the bracketed two terms of the arc-cosine expansion of Eqn (42) into Eqn (55) gives an approximate form more analogous to that of Eqn (54).

For  $0.7 < \chi < 1$ ,

$$\bar{M}_\alpha \doteq q S R \alpha C_{l\alpha} \left\{ \left[ \frac{1}{4} - \frac{1}{16\chi^2} \right] + \frac{\sqrt{2}\sqrt{1-\chi}}{2\pi} \left[ \frac{1}{4\chi^2} - 1 \right] + \frac{1}{4\pi} \sqrt{1-\chi^2} \left[ \frac{1}{2\chi} + \chi \right] \right\}. \quad (56)$$

By observation, Eqns (54 & 56) exhibit a smooth transition across  $\chi = 1$  for the rolling-moment due to angle-of-attack; this is expected and serves as a sanity check that the derivation for rolling-moment due to angle-of-attack may be correct.

#### *Coefficient of Total Rolling-Moment*

Combining Eqns (47, 54, 56), gives an expression for total rolling-moment and nondimensionalizing by  $(q S R)$  provides a time-averaged total rolling-moment coefficient for a boomerang based on blade element theory of:

$$\bar{C}_M \doteq \frac{1}{3} C_{l0} \chi + \alpha C_{l\alpha} \left\{ \left[ \frac{1}{4} - \frac{1}{16\chi^2} \right] \left[ 1 - \frac{2\sqrt{2}\sqrt{1-\hat{\chi}}}{\pi} \right] + \frac{\sqrt{1-\hat{\chi}^2}}{4\pi} \left[ \frac{1}{2\hat{\chi}} + \hat{\chi} \right] \right\}, \quad (57)$$

where  $\hat{\chi} = \min(\chi, 1)$  and Eqn (57) is appropriate for  $\chi \geq 0.7$ .

#### **Pitching-Moment Derivation**

Since cyclic lifting forces associated with BET are symmetric about the  $Y$ -axis, an integration for the time-averaged pitching-moment will always vanish. Hence,

$$\bar{C}_Y = 0. \quad (58)$$

Here  $\bar{C}_Y$  is the moment coefficient about the  $Y$ -axis (pitch direction).

Before we leave this section, we remind the reader that the BET derivations developed herein are based on non-tapered blades with zero off-set to the point of rotation. If the present boomerang theory is ever to be expanded upon, it should be done so with consideration to both of these geometric properties. However, even then, Eqn (58) will still hold. In order to achieve a non-zero  $\bar{C}_Y$ , downwash and/or wake effects must be included in the analysis. Until then, the lay-over phenomenon of boomerang dynamics cannot be explicitly studied. Nonetheless, the present work provides a good foundation in the understanding of boomerang aerodynamics. And although the investigations of Sections VII-VIII focus on time-averaged properties, the aerodynamic formulations of this section have been developed such that they can be utilized for time-accurate flight simulations of boomerangs with their actual mass properties of  $I_{11} \neq I_{22}$ .

In the next section, we will study various flight-path characteristics of a returning-type boomerang.

## **VII. Radius of a Boomerang's Flight Path**

Let's assume that it is possible for a boomerang to reach a time-averaged steady-state motion of level flight which forms, when viewed from above, a circular path of radius  $\mathcal{R}_p$ . Further, assume the boomerang rotation plane maintains a constant bank-angle of  $\theta$  during its flight. In this scenario, the precession rate of the boomerang rotation plane ( $\dot{\phi}$ ), times the radius of the circular flight path ( $\mathcal{R}_p$ ), must be equal to the velocity of the advancing boomerang ( $V$ ).

$$V = \dot{\phi} \mathcal{R}_p \quad (59)$$

For this same circular level flight path, the centrifugal acceleration is balanced by the horizontal component of the lift vector.

$$L \sin \theta = m \left( \frac{V^2}{\mathcal{R}_p} \right) \quad (60)$$

To sustain level flight, the vertical component of lift must balance the boomerang's weight.

$$L \cos \theta = m g \quad (61)$$

Here  $m$  is mass and  $g$  is gravitational acceleration. Strictly speaking, the equality of Eqn (61) must be enforced for level flight. In practice however, a fairly large departure from this state can occur. For example, consider playing catch with someone where a baseball is thrown back and forth. The path of the baseball is essentially a parabolic arc, as no lift is produced by the ball. The players of this game must throw the ball with initial velocity vectors appropriate for the path of the ball to intersect the receiver's position. In the case of a boomerang throw, while some lift in the vertical direction is being generated, it may not exactly balance the weight. Here, the thrower compensates the lift-weight imbalance simply by launching the boomerang slightly upwards to give just the right amount of time aloft for the boomerang to return. Because of this extra degree of freedom, Eqn (61) will not be enforced as a constraint in the current body of work.

Recall that Eqn (14) provides an approximation for the precession rate ( $\dot{\phi}$ ) in terms of rolling-moment ( $M_n$ ). If the boomerang is designed to fly at a negligible angle-of-attack, then the basic rolling-moment of Eqn (47) applies. Equating these relationships of rolling-moment and substitution of Eqn (59), gives the following sequence of equalities.

$$\begin{aligned} \left(\frac{1}{2}m R^2\right) \sin \theta \dot{\psi} \dot{\phi} &= \left(\frac{1}{2}\rho V^2\right) S R C_{l0} \left[\frac{\chi}{3}\right] \\ m R^2 \sin \theta \left(\frac{\chi V}{R}\right) \left(\frac{V}{\mathcal{R}_p}\right) &= \rho V^2 S R C_{l0} \left[\frac{\chi}{3}\right] \\ \frac{m \sin \theta}{\mathcal{R}_p} &= \frac{\rho S C_{l0}}{3} \end{aligned} \quad (62)$$

Rearranging Eqn (62) gives a compact derivation for the radius of the circular flight path.<sup>-3</sup>

$$\mathcal{R}_p = \left[ \frac{3 m \sin \theta}{\rho S C_{l0}} \right] \quad (63)$$

Remarkably, note that  $\mathcal{R}_p$  is independent of the boomerang's velocity ( $V$ ) or its rotational speed ( $\omega$ ). As a consequence, the radius of the boomerang's flight path can be set by design.

If we rearrange Eqn (60) for  $\mathcal{R}_p$  and substitute the basic lift given by Eqn (33), we can solve for an equilibrium value of  $\theta$  for a level circular flight path.

$$\sin^2 \theta = \left[ \frac{3}{4} + \frac{\chi^2}{2} \right]^{-1} \quad (64)$$

Amazingly, Eqn (64) draws a general conclusion which holds for any boomerang, regardless of mass or dimensional size! The only assumptions used to lead to this result are that the boomerang trims at  $\alpha = 0$ , its moment of inertia is  $I = \frac{1}{2}m R^2$ , that its flight path is level and that BET provides a reasonable aerodynamic model.

For a real solution of Eqn (64) to exist, the following condition regarding the boomerang's rotational velocity must hold.

$$\chi \geq \frac{\sqrt{2}}{2} \doteq 0.707 \quad (65)$$

Recall the predetermined initial state of a boomerang throw as described by Eqn (17). This relationship stated that  $\chi_0 \doteq 0.85$ . Now substitute this value of  $\chi_0$  into Eqn (64) to derive an initial inclination angle for the boomerang's orientation as it is being thrown.

$$\theta_0 \doteq 71.6^\circ \quad (66)$$

This result fits nicely within the range of applied experience as given by Eqn (16). Experience also has shown that  $\chi$  is not constant during boomerang flight; see Eqn (19). Considering this, it may be advantageous to combine Eqns (63-64) to define another relationship for the radius of a level, circular flight path.

$$\mathcal{R}_p = \left[ \frac{6 m}{\rho S C_{l0} \sqrt{3 + 2 \chi^2}} \right] \quad (67)$$

---

<sup>-3</sup>A similar conclusion can be drawn using Hess' aerodynamic model.



Therefore, from start to finish, as  $\chi$  increases, the flight-path radius ( $\mathcal{R}_p$ ) reduces. If the boomerang ever ends up near a hover mode where  $\theta \rightarrow 0$  and  $\chi \rightarrow \infty$ , it can rapidly precess such that this segment of its flight path will be a tight loop when viewed from above.

In Section IV is a discussion on bouncing a boomerang off the ground to induce a high-spin-rate flight. The example there showed that a value of  $\chi \doteq 3$  can be achieved if the velocity ( $V$ ) is reduced by 50% due to the impulse of the bounce. Through some experimentation, the author was able to achieve several such flights and managed to catch them on high-definition video. Qualitatively, the radius of these flight paths ( $\mathcal{R}_p$ ) is the same as that for a regular throw of the same boomerang when  $\theta \doteq 70^\circ$ . This observation is consistent with the implications of Eqn (63). During one of these flights, the bounce itself caused the boomerang to initially climb, then fall; from the thrower's view the path looked like a parabolic arc. However, about half-way down from its apex, the boomerang began to flare and adjust its attitude until it established an equilibrium flight path with a nominal sink rate. Measuring the inclination angle of the high-spin boomerang off video footage showed  $\theta \doteq 22^\circ$ . Although estimates for these velocities are rough, Eqn (64) nonetheless gives  $\theta_1 \doteq 25.9^\circ$  for  $\chi \doteq 3$ , which is in close agreement to that observed.

Conditions for static trim and dynamic stability are developed in the next section.

## VIII. Static Trim & Dynamic Stability

Consider a boomerang traveling in a level, circular flight path. Following a similar derivation as before for Eqns (62-64), one can determine a general relationship for the trim state to be:

$$(\bar{C}_M : \bar{C}_L) \equiv \frac{\bar{C}_M}{\bar{C}_L} = \left[ \frac{I}{m R^2} \right] \sin \theta \chi. \quad (68)$$

Here,  $\bar{C}_L$  and  $\bar{C}_M$  are the three dimensional, time-averaged lift and rolling-moment coefficients, respectively, and  $I$  is the moment of inertia. In general, the aerodynamic coefficients can be determined with BET equations, CFD simulation, or by experimental testing; it does not matter. However, note that this ratio is also a function of angle-of-attack; we will show that the condition for dynamic stability is:

$$\frac{d\left(\frac{\bar{C}_M}{\bar{C}_L}\right)}{d\alpha} < 0. \quad (69)$$

To illustrate why this is the case, for example, assume that a boomerang is initially thrown at a condition of  $\alpha = 0^\circ$ , whereas its trim state may occur at  $\alpha = 2^\circ$ . If the slope of the  $(\bar{C}_M : \bar{C}_L)$  curve is negative, then initially the  $(\bar{C}_M : \bar{C}_L)$  ratio will be too large for static trim. Because of this state of inequilibrium, the boomerang's precession rate will turn the rotation plane faster than the lateral component of lift turns the direction of flight; thus increasing the angle-of-attack of the rotation plane with respect to flight direction. This automatic adjustment will continue until the angle-of-attack reaches its trim value of  $\alpha = 2^\circ$  in this example. If this adjustment slightly over-shoots the trim condition, then the  $(\bar{C}_M : \bar{C}_L)$  ratio will be too small for static trim, now the horizontal lift component will turn the flight path faster than the rotation plane precesses and the angle-of-attack will be nudged back accordingly.

For the moment, consider  $\chi \geq 1$ . This will greatly simplify the following derivation for a condition of dynamic stability based on the BET aerodynamics model. Now substitute Eqns (44 & 57) into Eqn (68) and multiply numerator and denominator by  $48 \chi^2$  to obtain:

$$\frac{\bar{C}_M}{\bar{C}_L} = \frac{C_{l0} \left[ \frac{\chi}{3} \right] + \alpha C_{l\alpha} \left[ \frac{1}{4} - \frac{1}{16 \chi^2} \right]}{C_{l0} \left[ \frac{1}{2} + \frac{\chi^2}{3} \right] + \alpha C_{l\alpha} \left[ \frac{\chi}{2} + \frac{1}{4 \chi} \right]} = \frac{16 C_{l0} [\chi^3] + \alpha C_{l\alpha} [12 \chi^2 - 3]}{C_{l0} [24 \chi^2 + 16 \chi^4] + \alpha C_{l\alpha} [24 \chi^3 + 12 \chi]}. \quad (70)$$

Note that Eqn (70) is in the form:

$$\frac{\bar{C}_M}{\bar{C}_L} = \frac{a + b \alpha}{c + d \alpha}. \quad (71)$$

where,  $a$ ,  $b$ ,  $c$  and  $d$  are independent of  $\alpha$ . Differentiating Eqn (71) and applying the stability condition gives:

$$\frac{d\left(\frac{\bar{C}_M}{\bar{C}_L}\right)}{d\alpha} = \frac{b(c + d\alpha) - d(a + b\alpha)}{(c + d\alpha)^2} = \frac{(bc - ad)}{(c + d\alpha)^2} < 0. \quad (72)$$

Hence, if  $[bc < ad]$ , then the boomerang is dynamically stable. Assuming that  $C_{l0}$  and  $C_{l\alpha}$  are non-zero and positive, we have:

$$\begin{aligned} [12\chi^2 - 3] [24\chi^2 + 16\chi^4] &< [16\chi^3] [24\chi^3 + 12\chi] \\ [192\chi^4 + 240\chi^2 - 72] &< [384\chi^4 + 192\chi^2] \\ 0 &< [192\chi^4 - 48\chi^2 + 72] \end{aligned} \quad (73)$$

Eqn (73) always holds true, provided  $C_{l0} > 0$  and  $C_{l\alpha} > 0$ . However, at the beginning of this derivation thread, we assumed  $\chi \geq 1$  to simplify the mathematics. Therefore, we have only proven that boomerangs are dynamically stable for  $\chi \geq 1$  thus far. Nonetheless, dynamic stability seems to be an intrinsic property of the boomerang.

In the next section, a detailed boomerang geometry is developed as a test case for CFD analysis.

## IX. Boomerang Geometry

In this section, a boomerang design is developed for further CFD analysis. This configuration is representative of a starting point in a design process. Due to time limitations, no effort has been extended to improve upon this design... yet.

Figure 11 illustrates the general layout of the boomerang in planform view. Spanwise element lines are shown at quarter-chord intervals. Airfoil sections are depicted at five stations along the span of the boomerang. Note that the leading edge of the right blade is towards the top of the page, whereas the leading edge of the left blade is towards the bottom of the page. The twist distribution in this design is identically zero everywhere. This boomerang is designed to rotate counter-clockwise and is appropriate for a right-handed thrower. Because the airfoil sections flip direction, note that the centerline airfoil is symmetric front-to-back. The mid-chord lines of the trap planform are anchored to the origin at the centerline, their radial span is 12 inches and the angle between them is  $100^\circ$ . Note the curved planform near the centerline. Also shown in this figure is the center-of-mass location depicted by the asterisk symbol.

Figure 12 provides characteristics of the outboard airfoil sections, including thickness and camber distributions as well as airfoil geometry. The airfoil is 15% thick, with the maximum thickness occurring at 35% chord. The lower surface is flat from 2.5% to 97.5% chord. Both the leading and trailing edges have a radius of about 3% chord. The purpose of having a rounded trailing edge is that the airfoil is subjected to reversing onset flows during each cycle; refer back to Figures 8-10.

Reference quantities are provided in Table I. Mass properties are given in Table II.

Table I  
Reference Quantities

$C_{ref}$	2.00	<i>in</i>
$R_{ref}$	12.00	<i>in</i>
$S_{ref}$	59.80	<i>in</i> <sup>2</sup>
$\lambda$	0.67	
$\Lambda$	40.0°	
$S_{wet}$	125.60	<i>in</i> <sup>2</sup>
<i>Volume</i>	18.39	<i>in</i> <sup>3</sup>

Table II  
Mass Properties

$\rho_w$	0.0360	<i>slugs/in</i> <sup>3</sup>
$m$	0.0207	<i>slugs</i>
$X_{cg}$	3.1780	<i>in</i>
$I_{11}$	0.4320	<i>slugs-in</i> <sup>2</sup>
$I_{22}$	0.1020	<i>slugs-in</i> <sup>2</sup>
$I_{33}$	0.5340	<i>slugs-in</i> <sup>2</sup>
$R_g$	5.0780	<i>in</i>

Reference quantities are used in CFD calculations,  $\lambda$  is the taper ratio of the trap wing,  $\Lambda$  is the mid-chord sweep of the trap wing,  $S_{wet}$  is the surface-wetted area, *Volume* is the volume of the boomerang,  $\rho_w$  is the density of Australian mangrove wood,  $m$  is the boomerang's mass,  $X_{cg}$  is the  $X$ -location of the center-of-mass, the  $I$ 's are principal moments of inertia and  $R_g$  is the radius of gyration about the principal axis of rotation.

The results from 2D steady-state CFD solutions are discussed next.

## X. 2D Steady-State CFD Solutions

In this section, the boomerang airfoil developed in the previous section is analyzed using the OVERFLOW code. OVERFLOW<sup>8</sup> is a Reynolds-averaged Navier-Stokes method developed by NASA. The primary purpose of this 2D analysis is to determine  $C_{l0}$  and  $C_{l\alpha}$  values for the boomerang airfoil. These two quantities will be used in conjunction with BET Eqns (44 & 57) for comparison with the 3D CFD results in Section XI.

Figure 13 illustrates a close-up view of the O-mesh grid used for OVERFLOW calculations. Dimensions of this mesh are (257 x 97). The viscous spacing at the wall is  $\Delta y_1 = 0.0000125 C$  which is approximately  $\Delta y_1^+ = 1$ . Figure 14 provides pressure contours of the flowfield and depicts the pockets of flow separation with red streamlines. The flow condition shown here is  $Mach = 0.0774$  and  $\alpha = 0^\circ$ . Note the large region of flow separation at the trailing edge of the airfoil. This indicates that the initial airfoil specified for the boomerang section is probably much too thick. Figures 15-16 provide the lift curve and the drag polar for the boomerang airfoil, respectively. A least-squares linear fit of the lift curve gives:

$$C_{l0.2D} = 0.164 \quad , \quad C_{l\alpha.2D} = 4.433, \quad (74)$$

where the units of  $C_{l\alpha}$  are per radian.

As an alternative to the coefficients of Eqn (74), which are based on 2D CFD solutions, we also include a set of coefficients that use the form of BET, but are reverse-engineered from time-averaged 3D unsteady CFD simulations on the fine mesh, with  $\chi = 1$ . Fitting these data gives:

$$C_{l0.3D} = 0.262 \quad , \quad C_{l\alpha.3D} = 3.056. \quad (75)$$

Comparisons of 3D cyclic CFD calculations with BET estimates using both sets of coefficients will be provided in the next section.

## XI. 3D Unsteady CFD Simulations

This section provides numerical results for the boomerang configuration subjected to a forced rotary cyclic motion, submersed in uniform freestream flow. The freestream flow corresponds to 60 *mph* at sea-level conditions near Wagga Wagga, Australia;  $Mach = 0.0774$ ,  $Ren = 43,572$  and  $T = 538.5^\circ K$ . Air density at sea level is  $\rho = 1.3755 \times 10^{-6} \text{ slugs/in}^3$ . The aerodynamic database developed includes variations in rotational velocity and angle-of-attack.

A sequence of three volumetric meshes was generated for CFD computations. The fine mesh, with dimensions (257 x 169 x 97), was generated using the globally-elliptic meshing method of Vassberg.<sup>9,10</sup> Viscous spacing at the wall is  $\Delta y_1 = 0.000025 \text{ in}$  which is approximately  $\Delta y_1^+ = 1$ . Limited fine-mesh solutions were obtained due to their significant computational requirements, so medium and coarse meshes were also developed. Starting with the fine mesh, a medium mesh level was constructed by removing even-numbered computational planes of the fine mesh. This process is repeated using the medium mesh to create the coarse mesh. Dimensions of these meshes are (129 x 85 x 49) and (65 x 43 x 25), respectively.

Figure 17 illustrates a collection of truncated field planes near the boomerang surface. The predominately-vertical O-mesh planes wrapped around airfoil sections are J-planes. The horizontal planes at the boomerang leading and trailing edges are I-planes. The boomerang surface itself is the K=1 plane.

Figures 18-23 are a sequence of images which depict K-planes in ascending order. This grid is generated by starting with the boomerang surface (K=1) and extruding outwards to the farfield boundary. The farfield boundary is almost a perfect spherical surface and is about 100  $C_{refs}$  away from the boomerang; see Figure 23.

Figures 24-25 provide cyclic lift and rolling-moment coefficients for  $Mach = 0.0774$ ,  $\alpha = 0^\circ$  and  $\chi = 1$ . These data were computed on the fine mesh. The flowfield was initialized to freestream conditions and the forced cyclic motion of spinning the boomerang about its center-of-mass location was instantaneously started. The transients of this start-up process were allowed to sufficiently damp out, requiring 6 cycles. Hence, data presented herein is for the 7<sup>th</sup> cycle. To compare with BET, coefficients for the right and left blades are presented separately and have been shifted in phase by  $40^\circ$  and  $140^\circ$ , respectively. In these figures,  $\psi = 0^\circ$  corresponds to the angular position of each advancing blade when its mid-chord-line is perpendicular to the freestream flow. The BET results are shown as solid lines, whereas the CFD results for the right and

left blades are depicted as dashed lines with solid and open symbols, respectively. Note that BET captures the general trends of the CFD results, but not exactly. Further, the lifting (right) wing is shown to be more powerful than the dingle (left) wing, based on CFD. The reason is that the wake of the lifting wing has a much stronger influence on the dingle wing than vice-versa. One surprise revealed by these results is that BET, based on the 2D steady-state CFD coefficients of Eqn (74), under-predicts the lift and rolling-moment coefficients - usually the opposite occurs. However, in the case of 3D unsteady boomerang aerodynamics, cyclic reversals of flow direction over the airfoil sections, combined with large fluctuations of spanwise flow, work to keep the flow better attached to the boomerang's surface than predicted by 2D steady-state airfoil solutions, at least for  $\alpha = 0^\circ$ . Using the coefficients of Eqn (75) yields a much better agreement with 3D unsteady CFD results; these are depicted as solid lines with  $\times$  symbols in Figures 24-25.

Figures 26-38 provide a sequence of upper-surface isobars for the boomerang, again at flow conditions of  $Mach = 0.0774$ ,  $\alpha = 0^\circ$  and  $\chi = 1$ , for the 7<sup>th</sup> cycle. However, for these figures,  $\psi$  corresponds to the boomerang angular position, not the individual blades' position. This sequence begins at  $\psi = 0^\circ$  and steps forward in time at  $30^\circ$  intervals until the boomerang completes one full cycle, returning it to its initial position at  $\psi = 360^\circ$ . Note that the color spectrum of  $C_p$ -contours is held at a constant range of  $[-2, 0]$  over the duration of the spin cycle. Here, dark-blue contours depict  $C_p \doteq 0$ , while bright-red contours signify  $C_p \doteq -2$ . In these figures, the freestream flow is from left-to-right and the boomerang rotation is counter-clockwise. In general, the pressures on a retreating blade are close to  $C_p \doteq 0$ , while an advancing blade exhibits regions of flow where the pressures approach  $C_p \doteq -2$ , when it is nearly perpendicular to the freestream flow direction. Figures 27 & 31 show advancing blades near their peak lifting positions.

In order to develop an aerodynamic database for the boomerang, it was deemed necessary to run these cases on the coarse mesh. For reference, coarse-mesh transients sufficiently damp out within 3 cycles, so only a total of 4 cycles are required. This, in combination with the fact that the fine mesh is 64 times as large as the coarse mesh, reduces computational requirements by more than two-orders-of-magnitude.

Figure 39 illustrates the ratio of  $(\bar{C}_M : \bar{C}_L)$ , as predicted by CFD on the coarse mesh. The significance of this relationship between the lift and rolling-moment coefficients is two-fold. Firstly, it establishes trimming conditions on  $\alpha$  as a function of  $(\chi, \theta)$ , per Eqn (68). Secondly, it shows the boomerang to be dynamically stable because its slope is negative. For example, consider a condition of  $\chi = 1.2$  and  $\theta = 70^\circ$ . Recall the boomerang's values of  $I = 0.534 \text{ slug in}^2$ ,  $m = 0.0207 \text{ slugs}$  and  $R = 12 \text{ in}$ . Plugging these into Eqn 68 gives a required  $(\bar{C}_M : \bar{C}_L)$  ratio of 0.202. Hence, under these conditions, the boomerang will trim at  $\alpha \doteq 2.5^\circ$ . Furthermore, not only will it trim at this condition, it will be dynamically stable, per Eqn (69).

Figures 40-41 provide time-averaged values of lift and rolling-moment coefficients as a function of angle-of-attack, respectively. BET results are depicted by solid lines while CFD data (as computed on the coarse mesh) are given as solid symbols on dashed lines. Note that "BET-2D" (based on 2D steady-state CFD coefficients) under-predicts the lift at small angles-of-attack, but then over-predicts it at  $\alpha > 3.4^\circ$ , whereas it over-predicts the rolling-moment at all conditions run with CFD. The "BET 3D" data is based 3D unsteady CFD solutions on fine-mesh. BET 3D predicts a slightly-higher level of lift than CFD does on the coarse mesh. Further, it predicts a much larger rolling-moment than CFD does. This is probably due to blade taper and off-set effects which are not captured by BET derivations herein.

## XII. Coupled CFD-6DOF Simulations

A very preliminary numerical simulation of a boomerang flight has been performed using the six-degree-of-freedom (6DOF) capability of OVERFLOW. For this flight, the environmental condition has a wind blowing in the  $X$ -direction at  $5 \text{ mph}$ . The boomerang is launched from the origin with an initial velocity of  $V_0 = 60 \text{ mph}$  and rotational speed of  $\omega_0 = 88 \text{ rad/sec}$ , corresponding to  $\chi_0 = 1$ . The heading of the throw is directly out the  $Y$ -axis and  $30^\circ$  upward. The initial inclination angle of the boomerang's axis of rotation is  $\theta = 75^\circ$ . Note that this throw is perpendicular to the wind direction. In addition, the thrower is right-handed and the expected path from his point-of-view is for the boomerang to curve left into the wind, make a full circle and return.

Figure 42 provides a four-view of the computed flight path depicted as solid lines with asterisk symbols and encapsulated by a box with 2,000-inch sides. For reference, the sole asterisk in the center of the box is located at  $(X, Y, Z) = (-1000, 1000, 1000)$  inches. Now focus on the top-left quadrant of this figure where

the image is a view from above. In this quadrant, the wind is coming from the top of the page and the boomerang is thrown to the right from the origin which is located at the bottom-left corner of the square. Also provided in this view is a circular arc of radius 2,783 inches; this is the value of  $\mathcal{R}_p$  as estimated by Eqn (63). It is incredible how similar the flight path of the numerical simulation matches the predicted circular path at point of launch. Furthermore, as the boomerang flight progresses and  $\chi$  increases, the radius of the 6DOF flight path is reduced. This characteristic of the flight path tightening is qualitatively predicted by Eqns (19 & 67). In this simulation, the boomerang reaches out almost 2,600 inches, climbs to a height of about 1,400 inches and returns about half-way before making contact with the ground. Although this numerical flight is far from perfect, it exhibits behavior that verifies BET predictions.

Figure 43 provides a stereoscopic pair of images for the oblique view of Figure 42. In order to view this figure in 3D, hold the page about 12" away from the eyes and stare deeply into the images until they merge in the center. Adjustment fore-and-aft may be necessary to pull the view into focus.

### XIII. Summary and Conclusions

A new aerodynamic model has been developed using Blade Element Theory for the purpose of investigating aerodynamic characteristics and flight dynamics of boomerangs. This represents a substantial advancement of boomerang study. The new theory leads to some significant findings regarding the radius of a boomerang's circular flight path, the required inclination angle of its axis-of-rotation, its trim state, as well as its dynamic stability. Further, a lower bound on tip-speed-ratio exists ( $\chi \geq 0.707$ ) for a boomerang to trim statically. For a boomerang to be dynamically stable, its lift at no angle-of-attack must be positive. These discoveries provide a basic understanding of how the interplay between aerodynamic forces and moments, and gyroscopic precession combine to return the boomerang to its rightful owner by way of a circular flight path.

A V-shaped boomerang design has been used as a case study for detailed analyses. Unsteady Reynolds-averaged Navier-Stokes solutions provide accurate three-dimensional aerodynamic characteristics of the subject boomerang. These results are compared with BET predictions which illustrate that BET captures the essence of CFD results, but not exactly their full details. A high-fidelity CFD-6DOF simulation of a boomerang flight has been performed. Although preliminary, this result verifies that BET, coupled with gyroscope equations of motion, can accurately predict the radius and other characteristics of a boomerang's flight path.

Performing accurate BET-6DOF flight simulations should also be possible as BET captures the essential features of cyclic forces and moments, however, with the caveat that its cyclic pitching-moment integrates to zero. Nonetheless, these simulations can be performed faster than real time whereas CFD-6DOF cannot. Future work by the author will include developing BET-6DOF numerical flight simulation technology to study boomerang trajectories.

The theory developed in this body of work provides a formal methodology for customizing future boomerang designs. With knowledge of this theory, it is clear in retrospect that the case-study boomerang developed herein should be redesigned with the following features. Reducing thickness of its airfoil sections will reduce mass, flow separation and drag. Increasing curvature immediately at the leading and trailing edges will better facilitate the Kutta condition, whether the flow is reversed or not. Less flow separation and improved Kutta condition will effectively increase lift at no angle-of-attack. These will all combine to reduce the radius of the flight path which is currently much too large for practical use.

### XIV. Acknowledgements

The author thanks Neal Harrison, Dylan Vassberg and Jessee Ramirez for their help in this endeavor. Neal volunteered significant personal time for CAD support and CFD processing. Jessee provided high-definition camera gear and personal time to film our boomerang flight tests. Dylan converted many takes of raw video into polished movie clips; he strategically edited out his bloopers, yet methodically retained those of the author.

The author also acknowledges and thanks the proof readers of this paper: Blaine Rawdon, Andrew Killeen, Antony Jameson, Neal Harrison, Anthony Scalfani, Brian Vassberg, Dylan Vassberg and Claire Vassberg.

## References

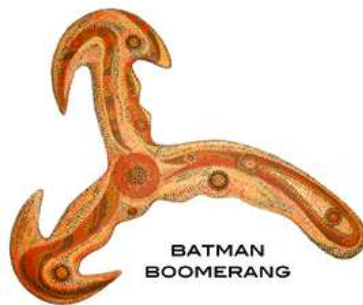
- <sup>1</sup>R. D. Lorenz. *Spinning Flight*. Springer, New York, 2006.
- <sup>2</sup>J. B. Mauro. *An Introduction to Boomerangs*. Smith & Flannery, Inc., Richmond, VA, 1989. Third Edition.
- <sup>3</sup>M. J. Hanson. *The Boomerang Book*. Puffin Books, Harmondsworth, Middlesex, England, 1974.
- <sup>4</sup>Unknown. Boomerang. <http://en.wikipedia.org/wiki/Boomerang>, June 2012.
- <sup>5</sup>W. E. Wiesel. *Spaceflight Dynamics*. McGraw-Hill, New York, 1997. Second Edition.
- <sup>6</sup>Unknown. light-up-boomerang.jpg. <http://www.geekologie.com/2007/09/>, June 2012.
- <sup>7</sup>F. Hess. The Aerodynamics of Boomerangs. *Scientific American*, 219:124–136, September 1968.
- <sup>8</sup>P. G. Buning, D. C. Jespersen, T. H. Pulliam, W. M. Chan, J. P. Slotnick, S. E. Krist, and K. J. Renze. OVERFLOW user’s manual, version 1.8l. *NASA Report*, NASA Langley Research Center, Hampton, VA, 1999.
- <sup>9</sup>J. C. Vassberg. Multi-block mesh extrusion driven by a globally elliptic system. *Conference Proceedings*, 5<sup>th</sup> U.S. National Congress on Computational Mechanics, 2<sup>nd</sup> Symposium on Trends in Unstructured Mesh Generation, Boulder, CO, August 1999.
- <sup>10</sup>J. C. Vassberg. Further study of globally elliptic meshing. *Conference Proceedings*, 7<sup>th</sup> International Conference on Numerical Grid Generation in Computational Field Simulations, Whistler, British Columbia, Canada, September 2000.



# ABORIGINAL WARRIORS WITH EARLY 20TH CENTURY BOOMERANGS



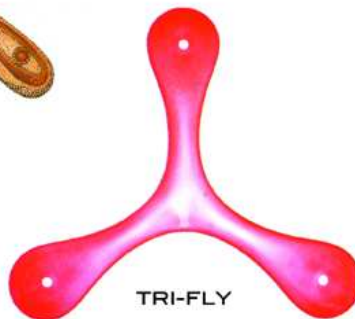
Figure 1. Aboriginal Boomerangs.



## MODERN-DAY BOOMERANGS



L.E.D.  
BOOMERANG



MODERN  
ABORIGINAL



Figure 2. Modern-Day Boomerangs.

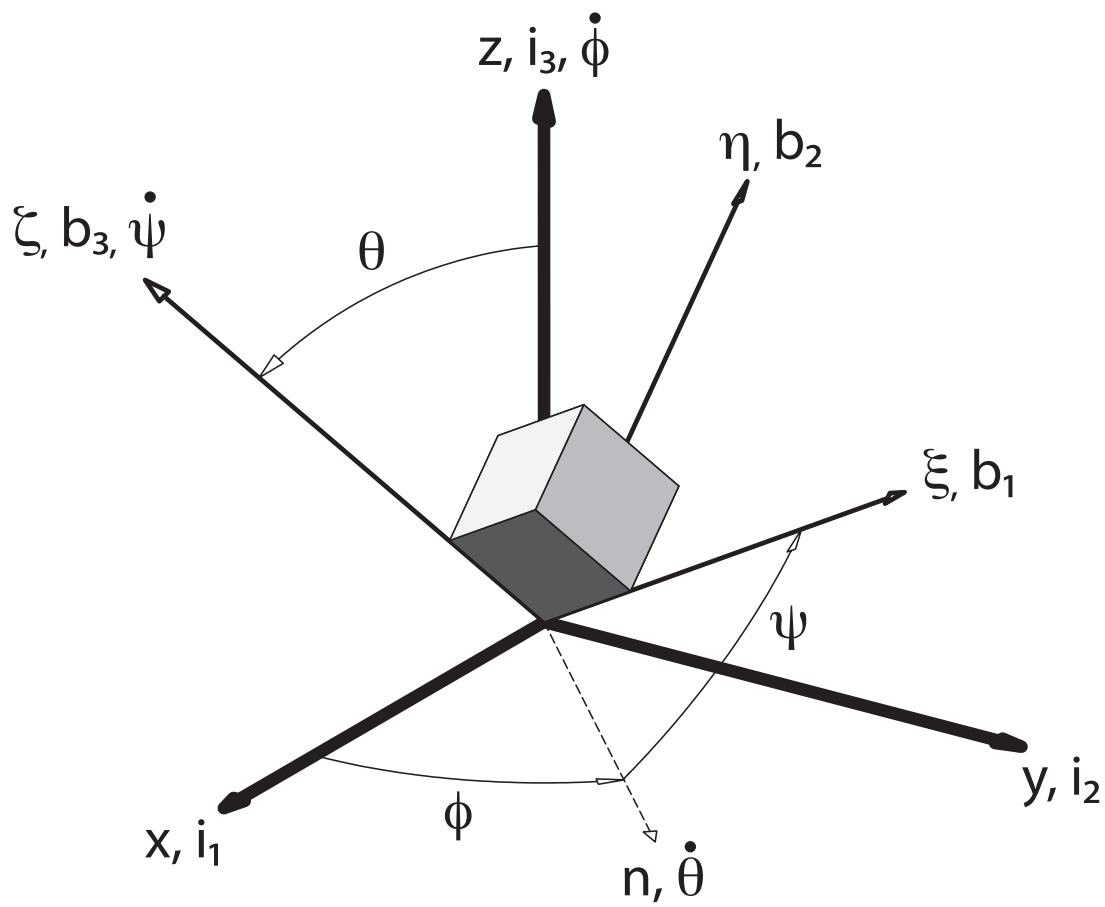


Figure 3. Classical Euler Angles:  $\phi$ ,  $\theta$ ,  $\psi$ .

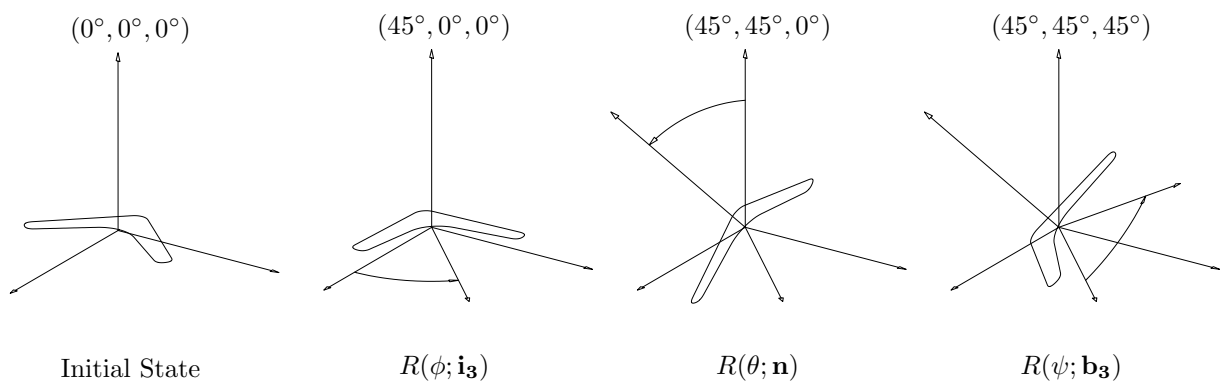


Figure 4. Rotation Sequence to Transform Boomerang to  $(\phi, \theta, \psi) = (45^\circ, 45^\circ, 45^\circ)$ .



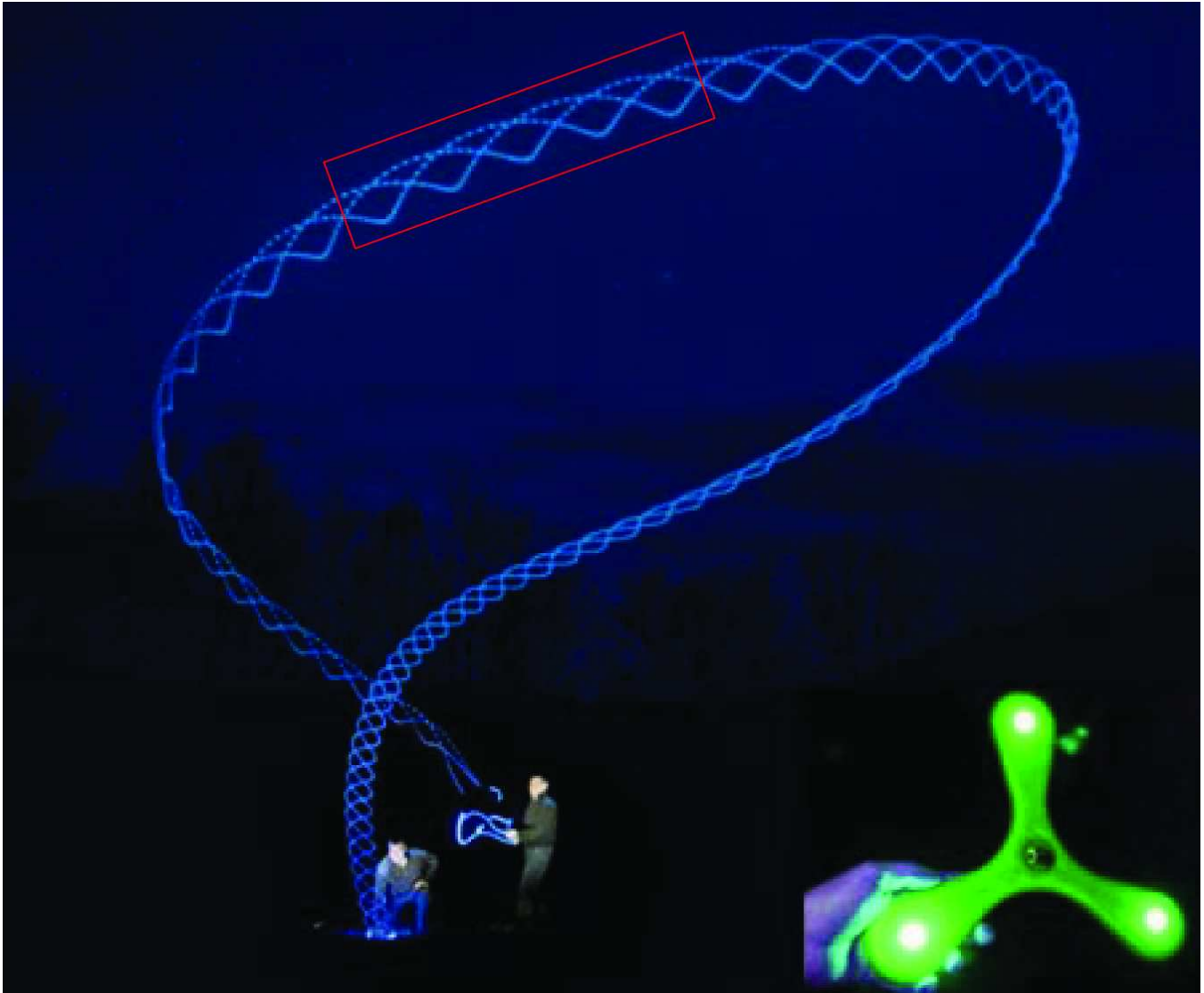


Figure 5. Boomerang Strobed Night Flight.

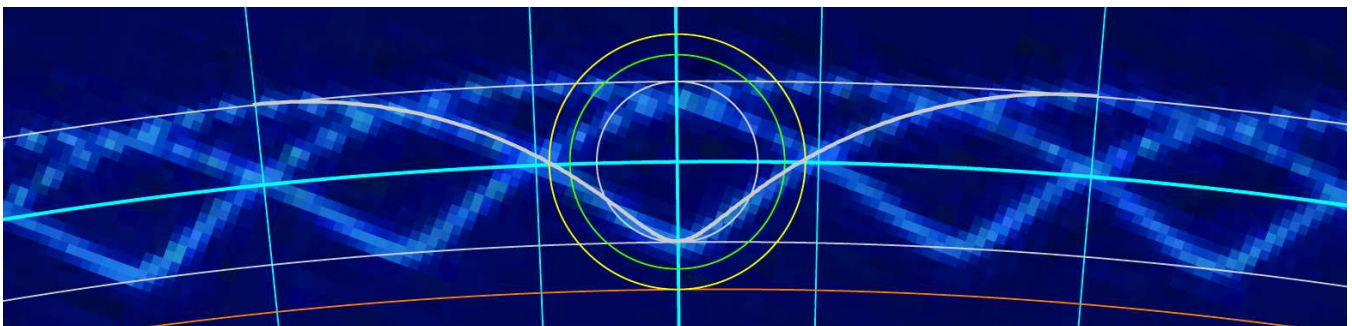


Figure 6. Hypo-Cycloid Analysis of Boomerang Night Flight;  $\chi = 0.85$ .

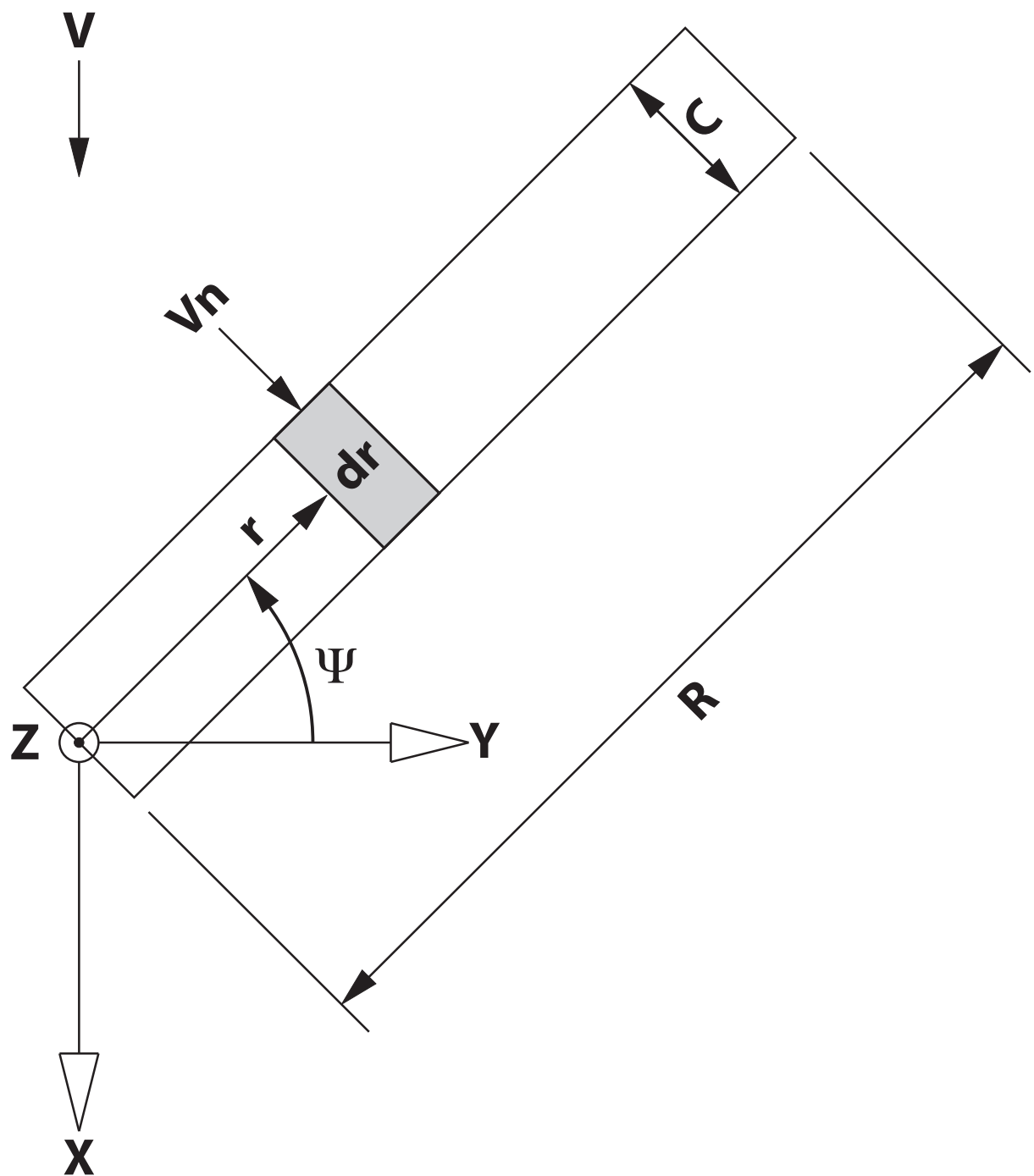


Figure 7. Blade Element Theory Schematic.

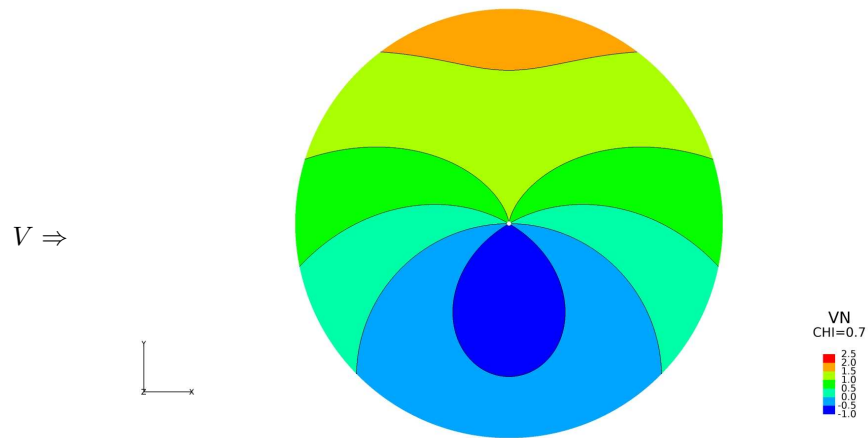


Figure 8.  $V_n$  Contours in the Rotation Plane;  $\chi = 0.7$ .

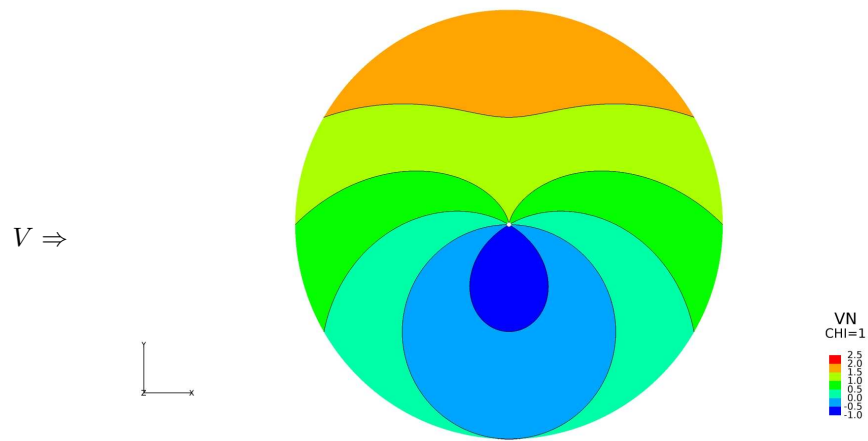


Figure 9.  $V_n$  Contours in the Rotation Plane;  $\chi = 1.0$ .

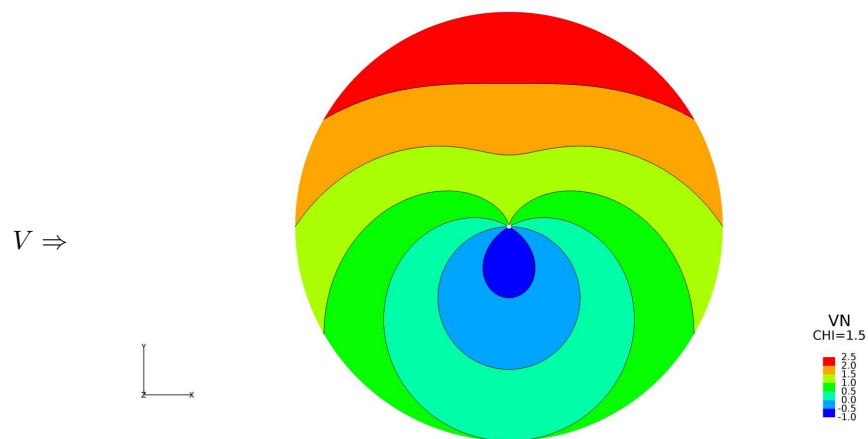


Figure 10.  $V_n$  Contours in the Rotation Plane;  $\chi = 1.5$ .

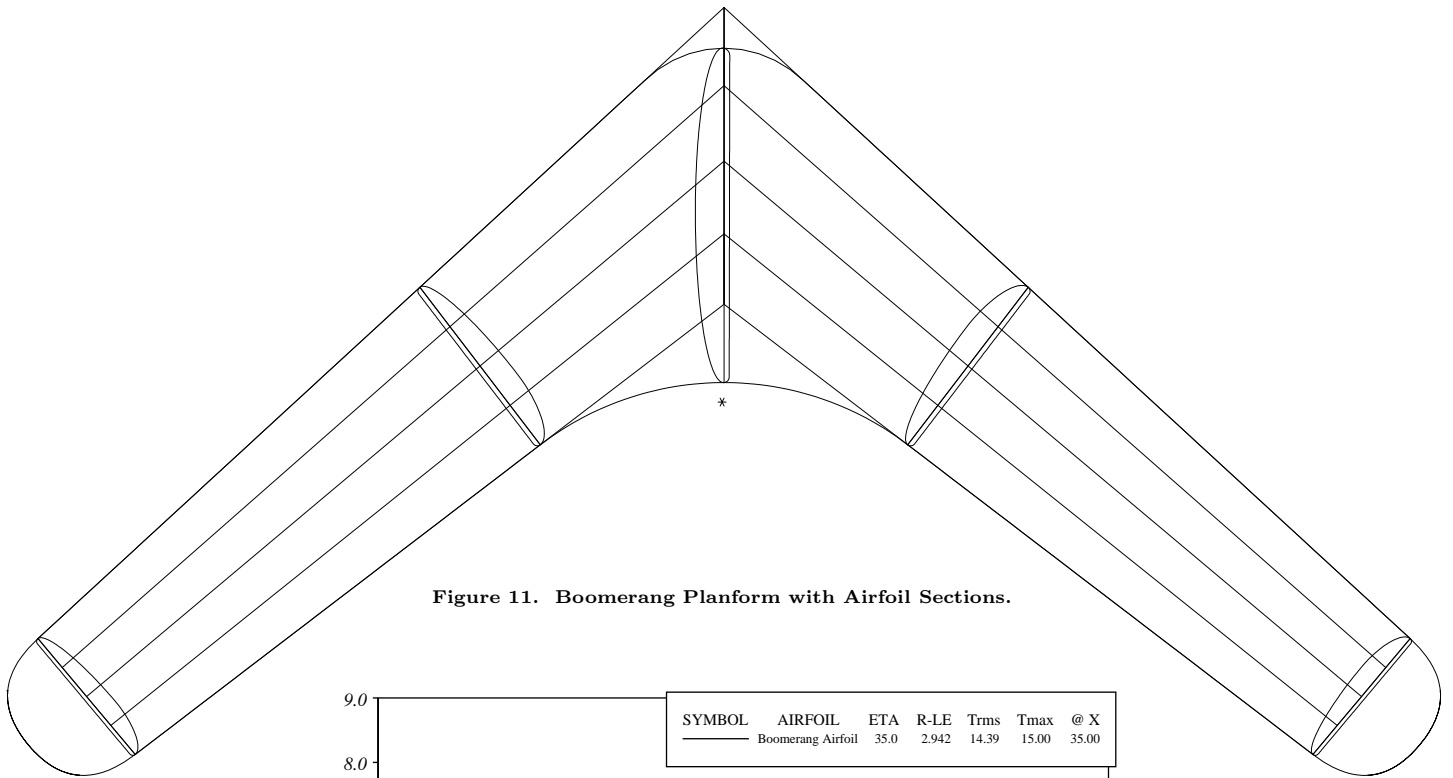


Figure 11. Boomerang Planform with Airfoil Sections.

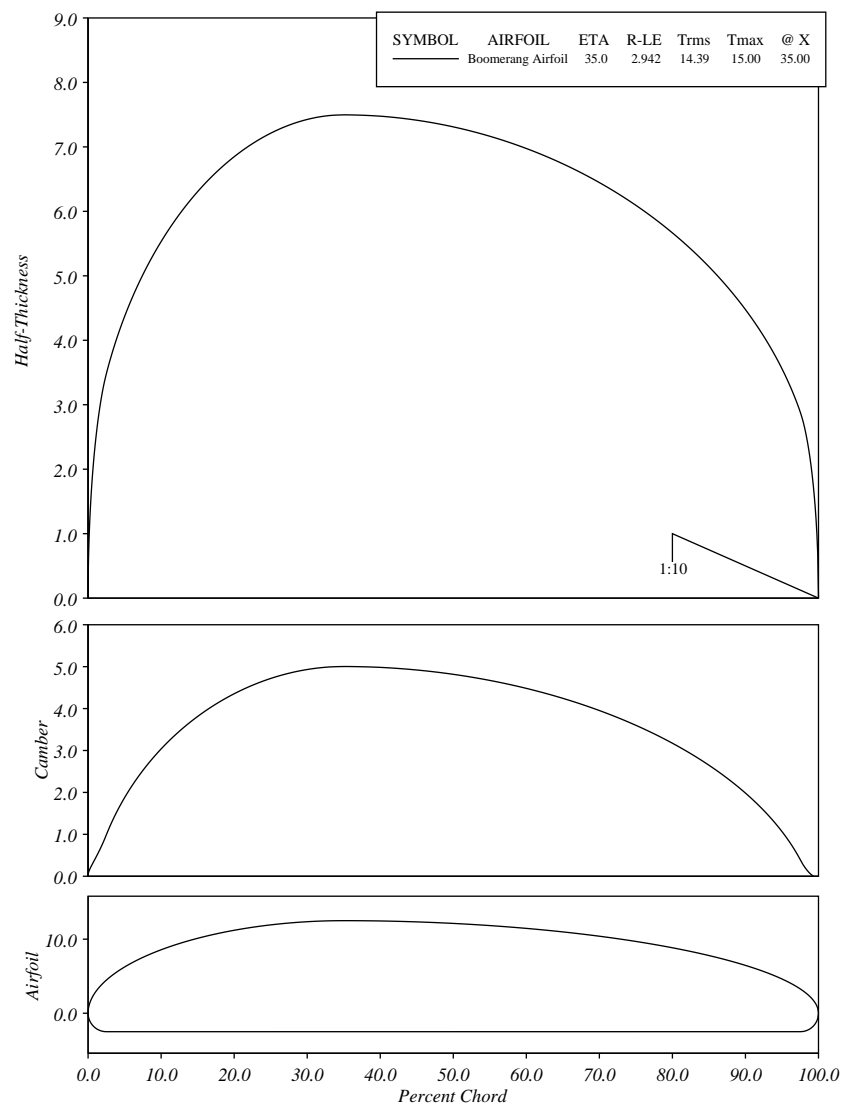


Figure 12. Boomerang Airfoil Geometry, Camber & Thickness Distributions.

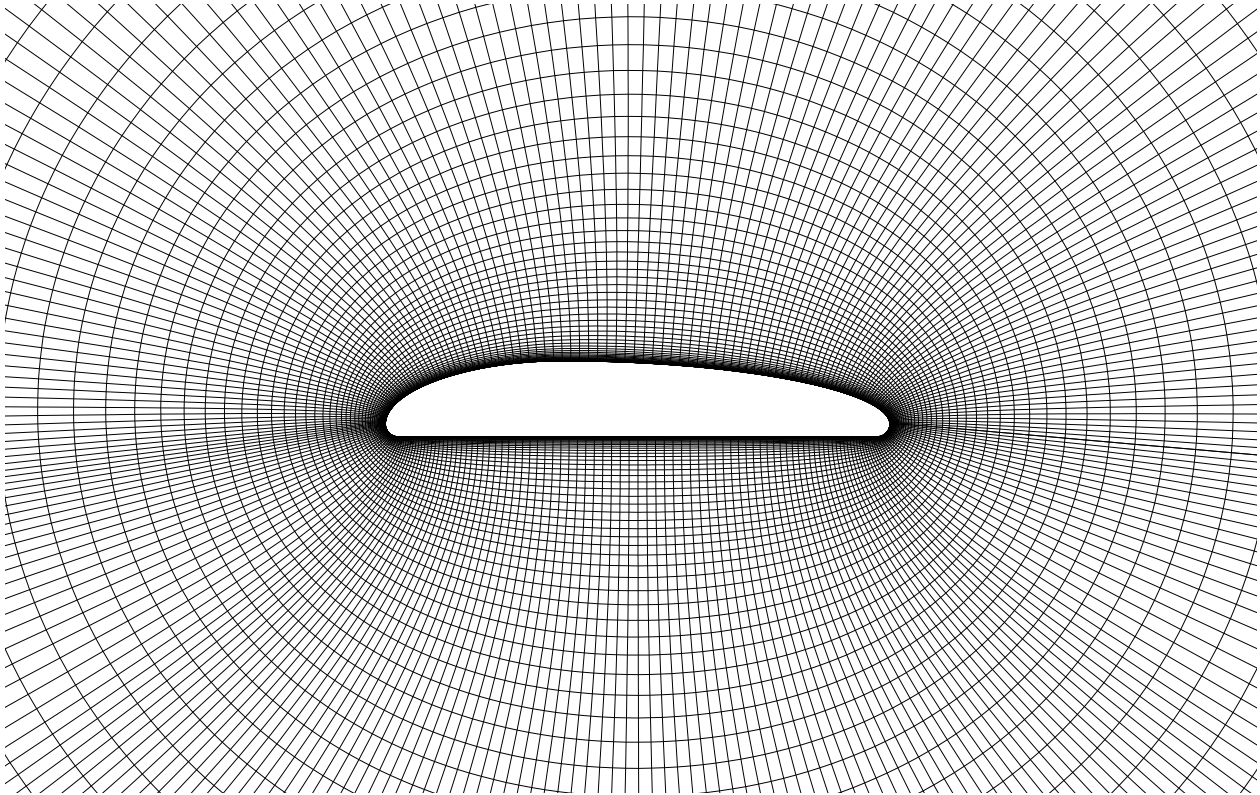


Figure 13. Boomerang Airfoil Grid; (257x97) O-Mesh.

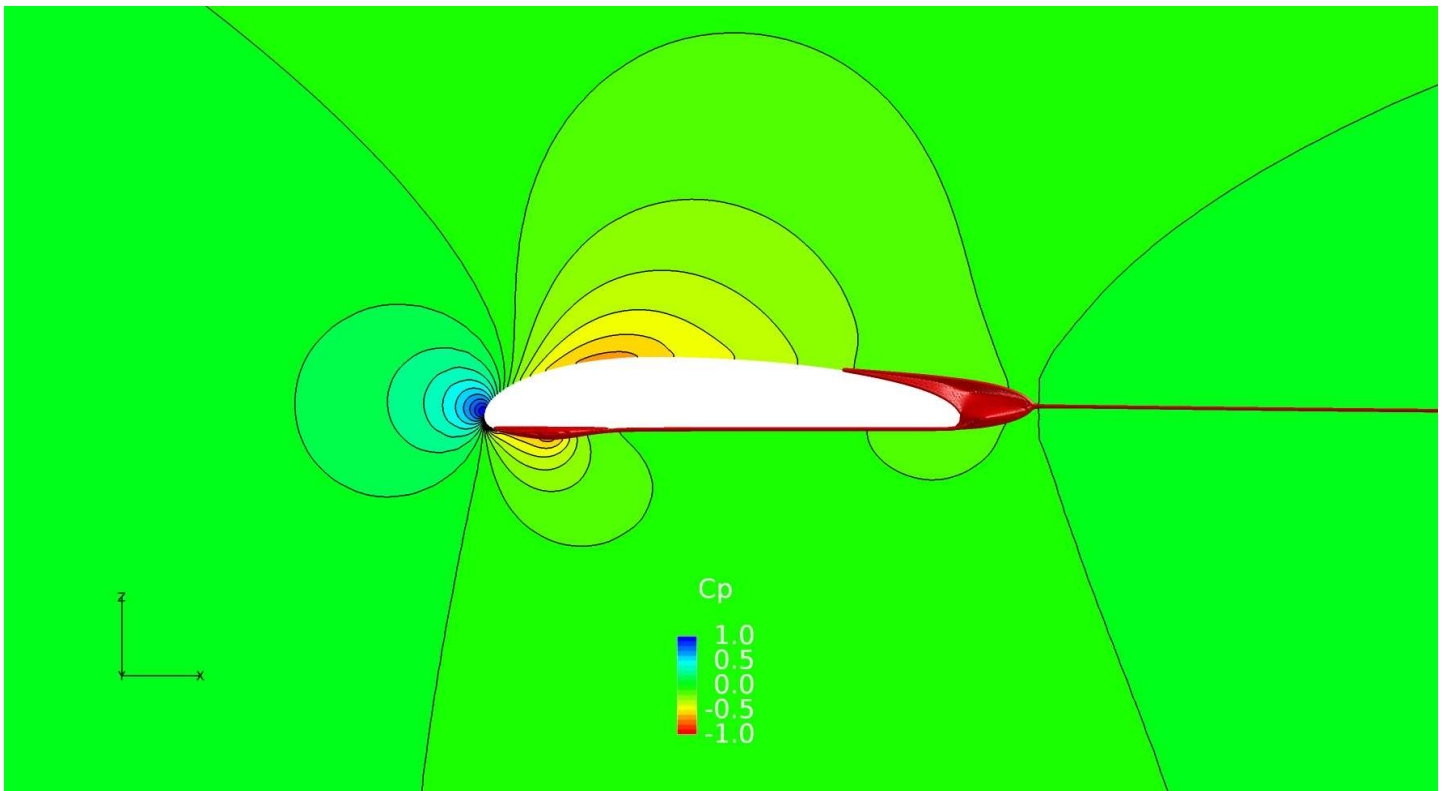


Figure 14. Boomerang Airfoil Field Cp-Contours and Separation Bubbles;  $Mach = 0.0774$ ,  $Ren = 43,572$ ,  $\alpha = 0$ .

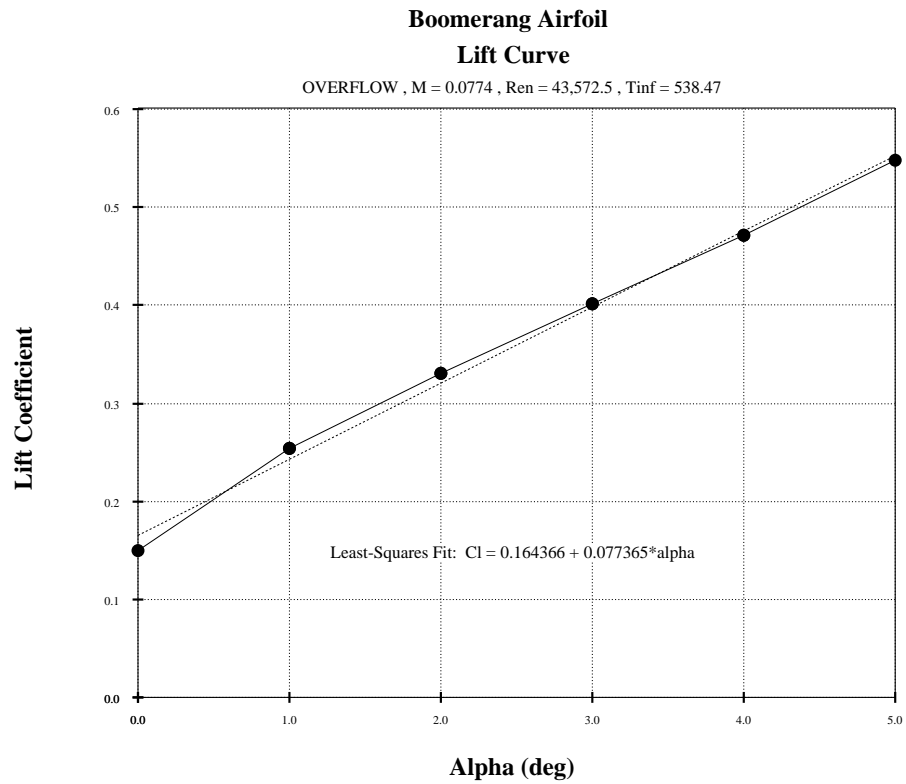


Figure 15. Boomerang Airfoil Lift Curve;  $M = 0.0774$ ,  $Re = 43,572$ .

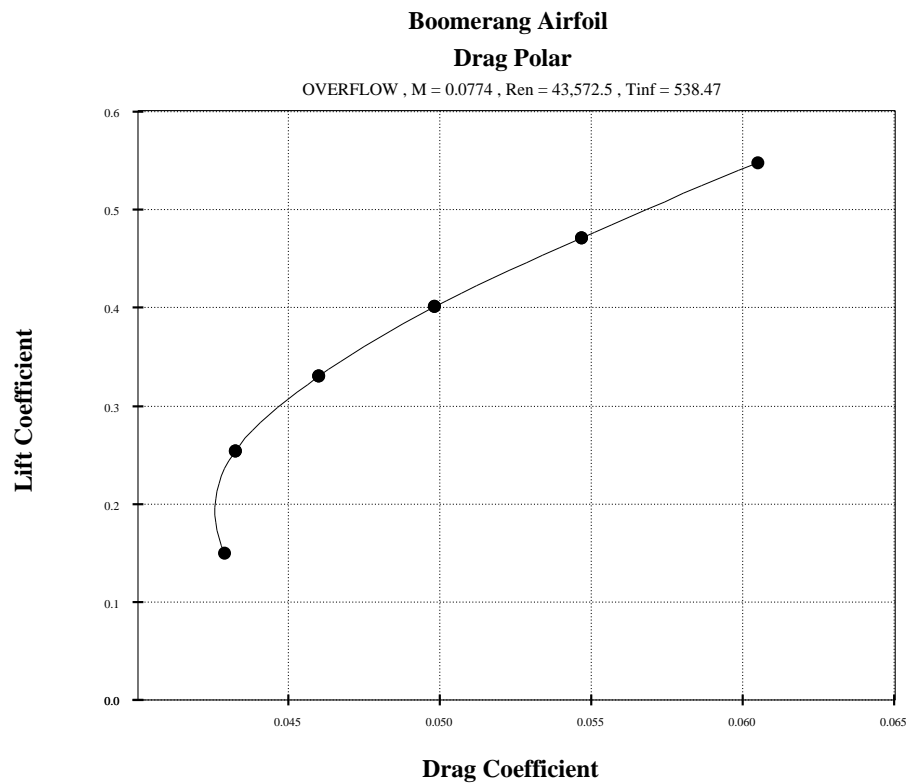


Figure 16. Boomerang Airfoil Drag Polar;  $M = 0.0774$ ,  $Re = 43,572$ .

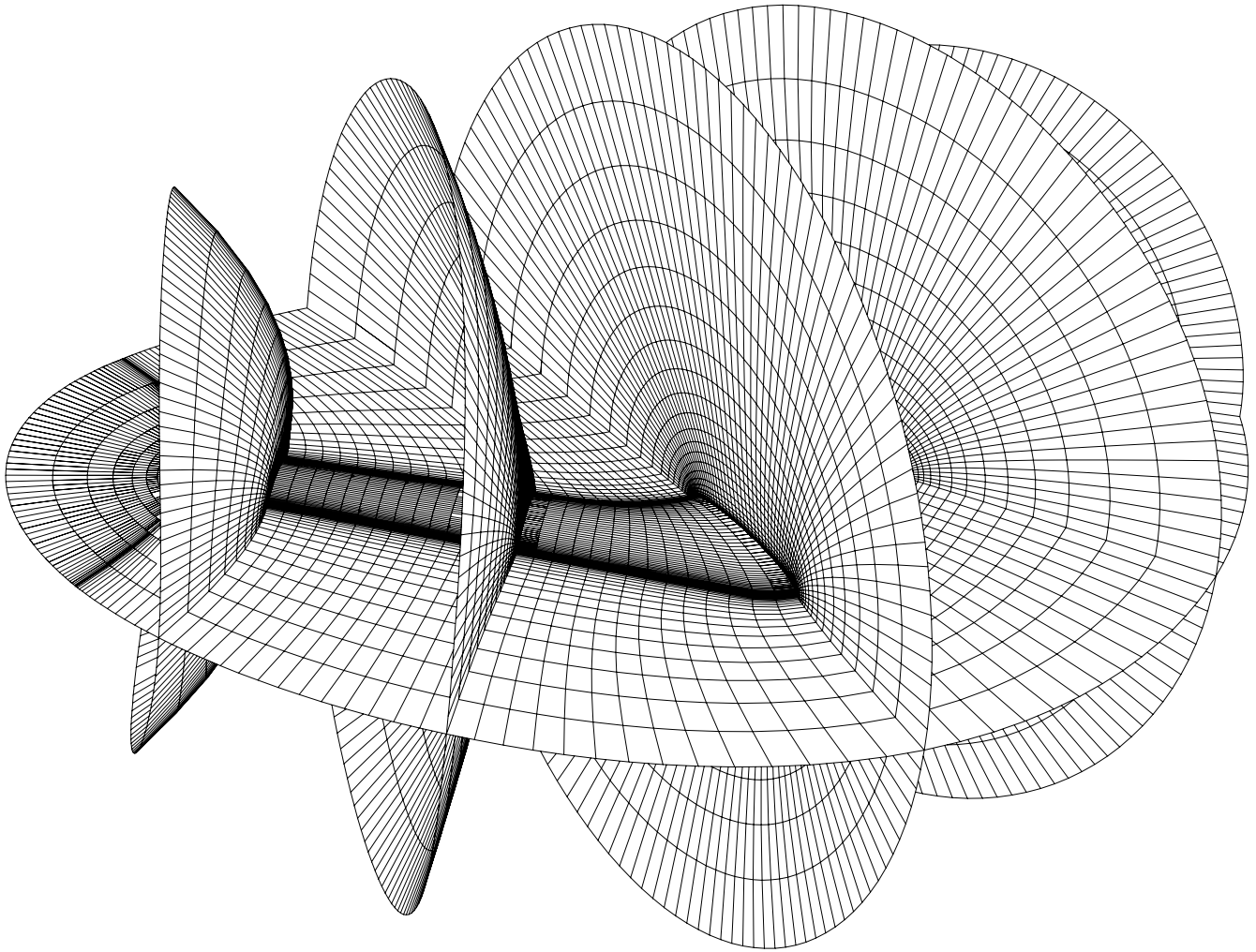


Figure 17. Boomerang Near-Field Grid with ILE-Plane, ITE-Plane & Several J-Planes.

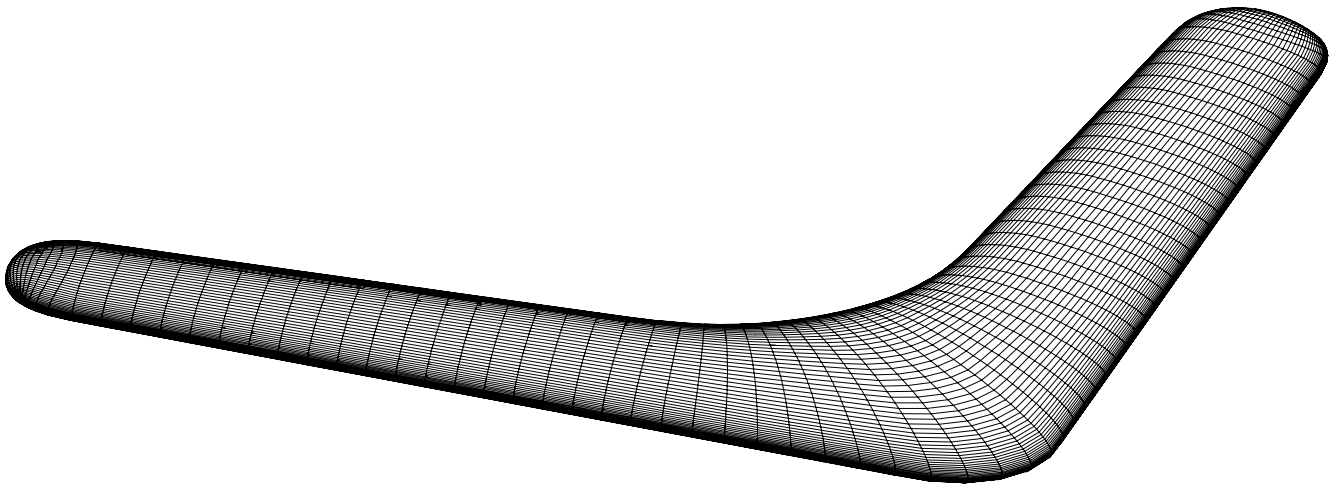


Figure 18. Boomerang Surface Grid;  $K=1$  Plane.

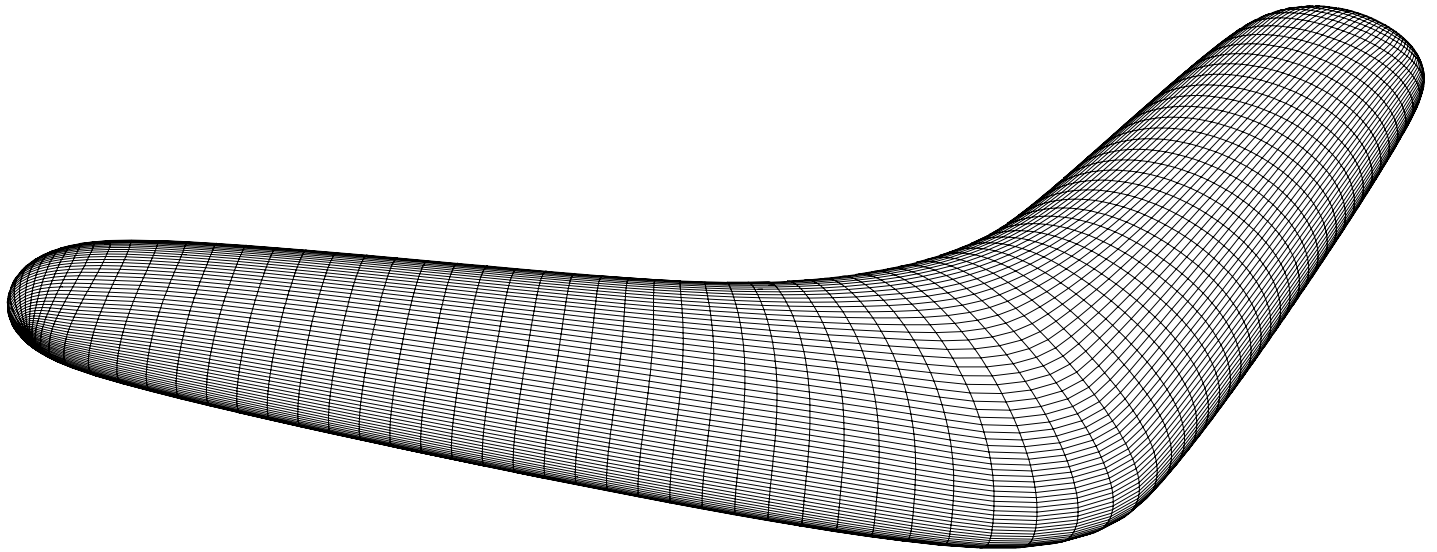


Figure 19. Boomerang Field Grid;  $K=25/49$  Plane.

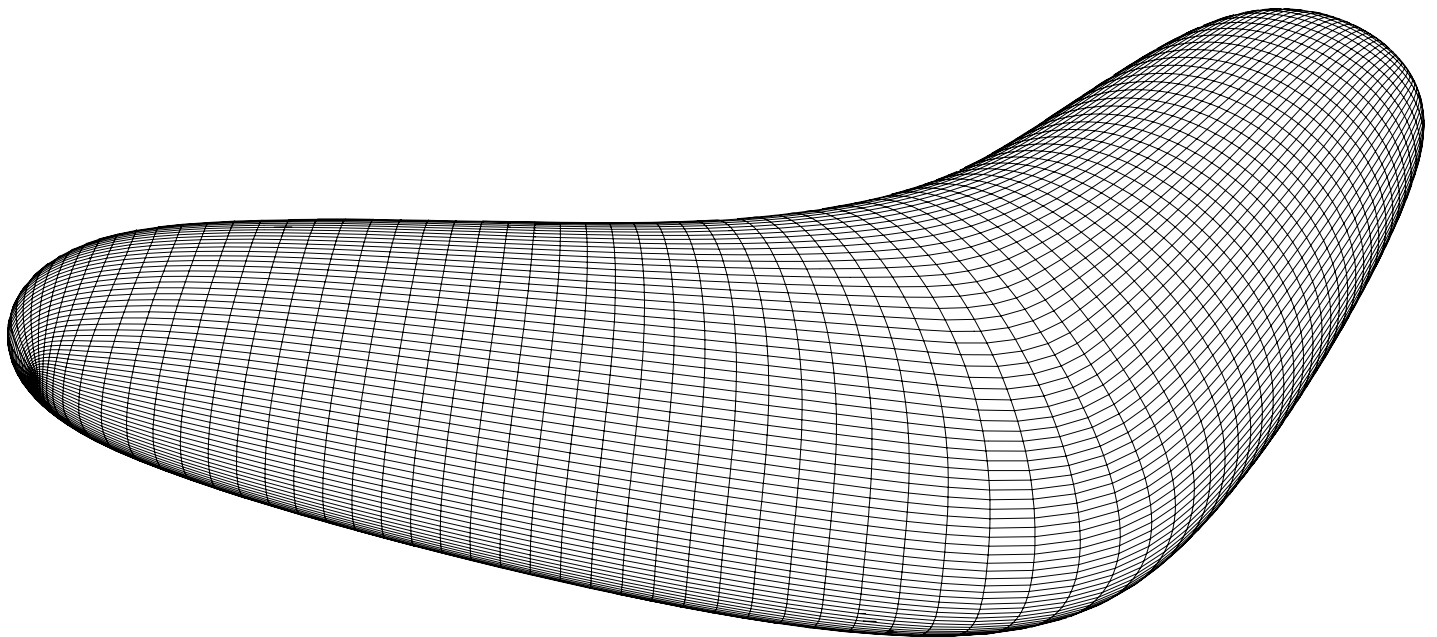


Figure 20. Boomerang Field Grid;  $K=29/49$  Plane.



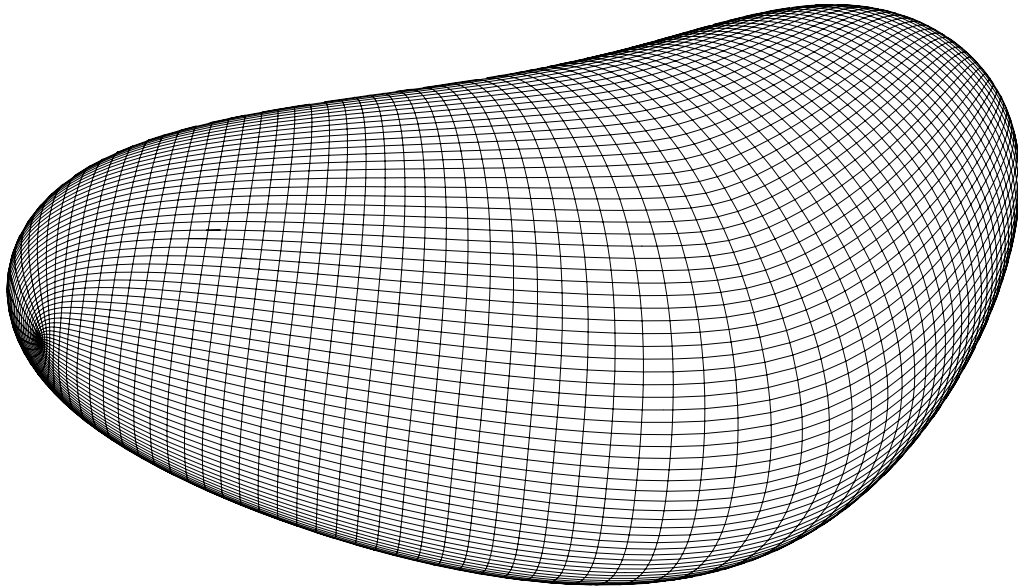


Figure 21. Boomerang Field Grid;  $K=33/49$  Plane.

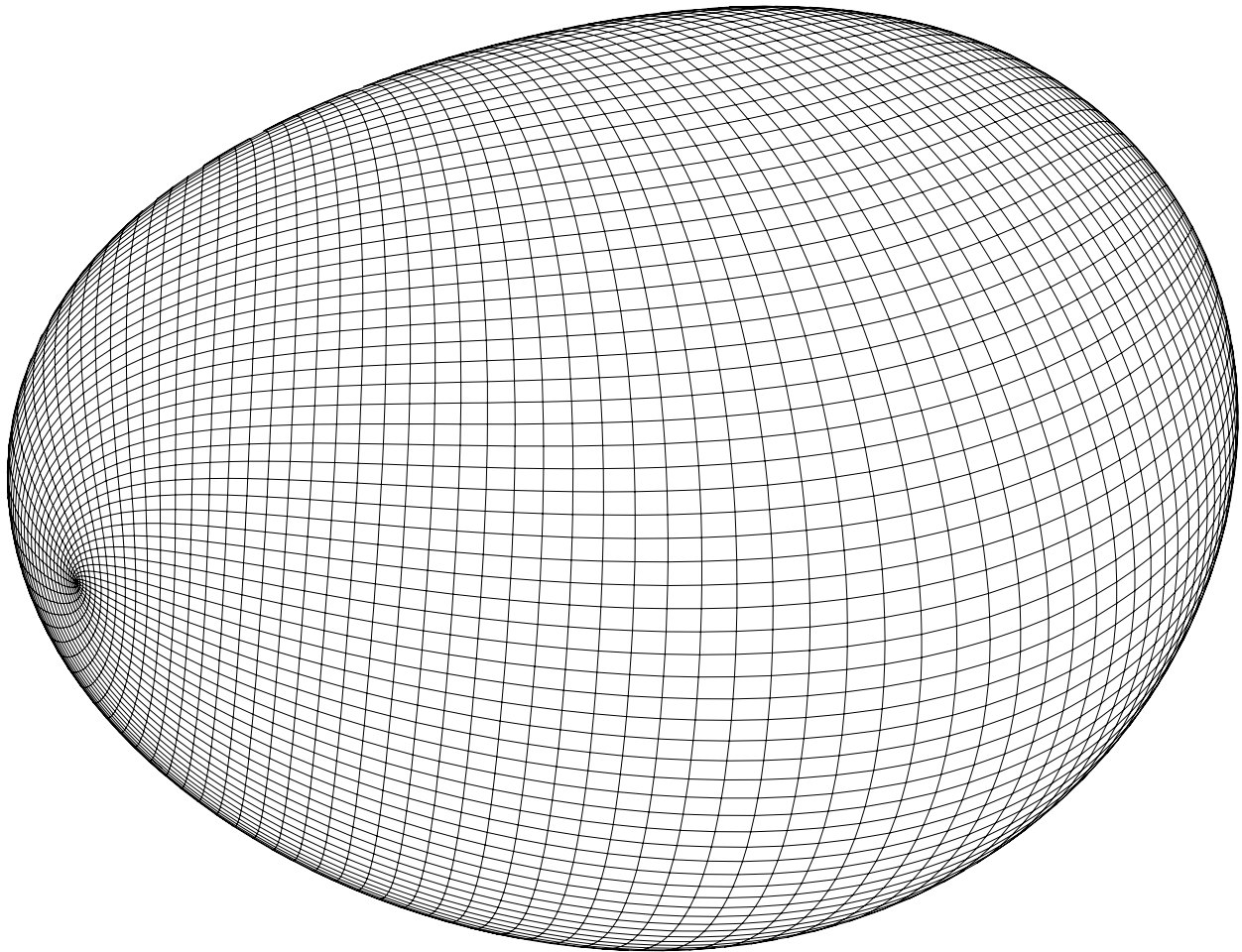


Figure 22. Boomerang Field Grid;  $K=37/49$  Plane;  $\sim 5$ -Crefs Out.

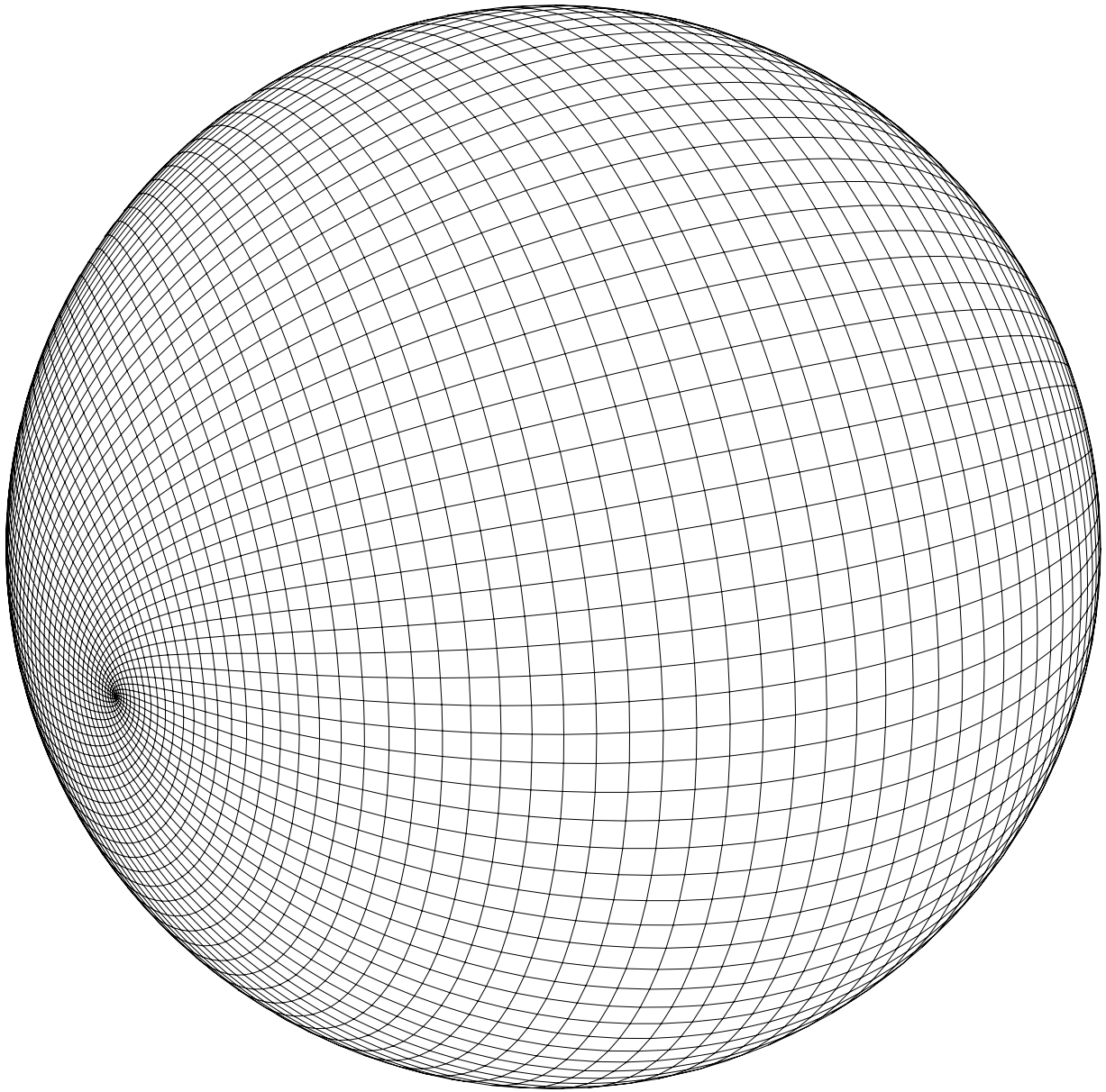


Figure 23. Boomerang Far-Field Boundary;  $K=49/49$  Plane;  $\sim 100$ -Crefs Out.

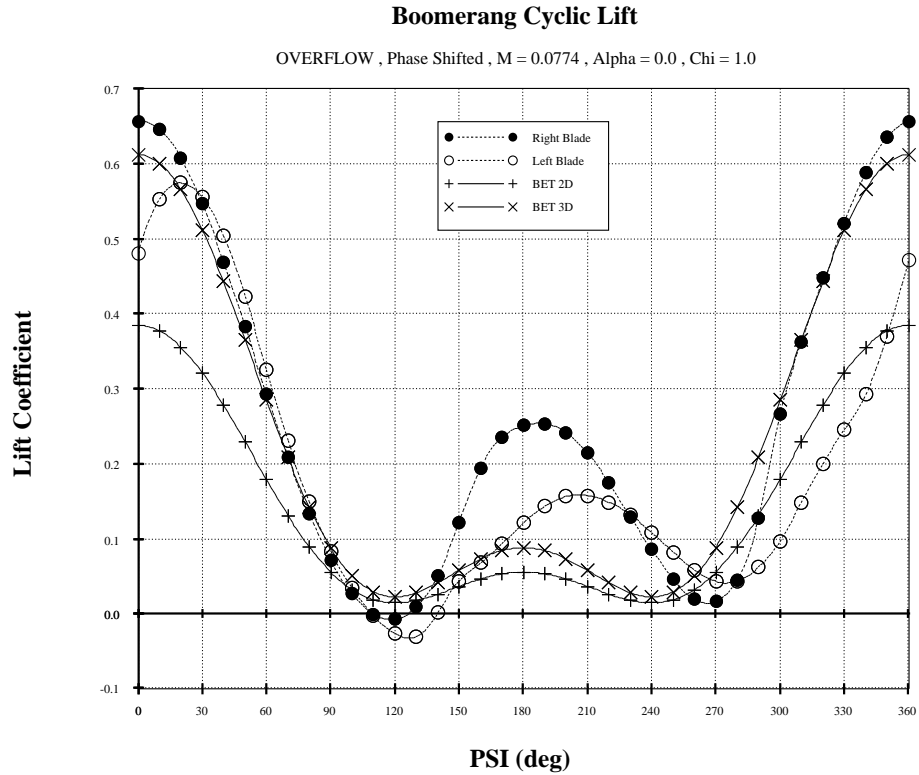


Figure 24. Boomerang Phase-Aligned Cyclic Lift;  $Mach = 0.0774$ ,  $Re = 43,572$ ,  $\chi = 1.0$ ,  $\alpha = 0$ .

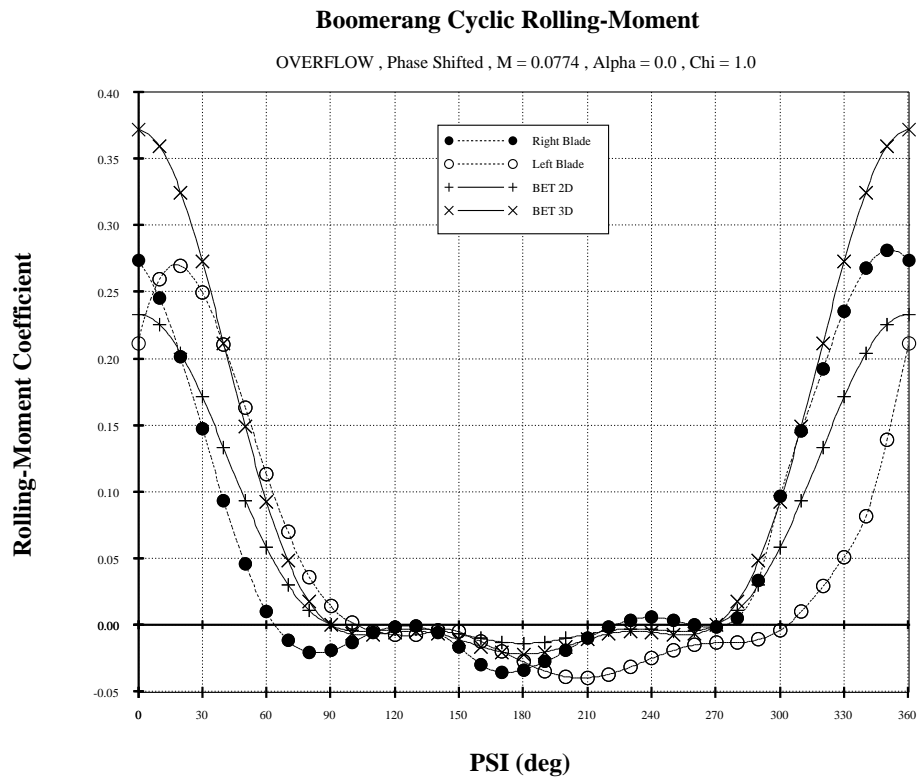


Figure 25. Boomerang Phase-Aligned Cyclic Rolling-Moment;  $Mach = 0.0774$ ,  $Re = 43,572$ ,  $\chi = 1.0$ ,  $\alpha = 0$ .

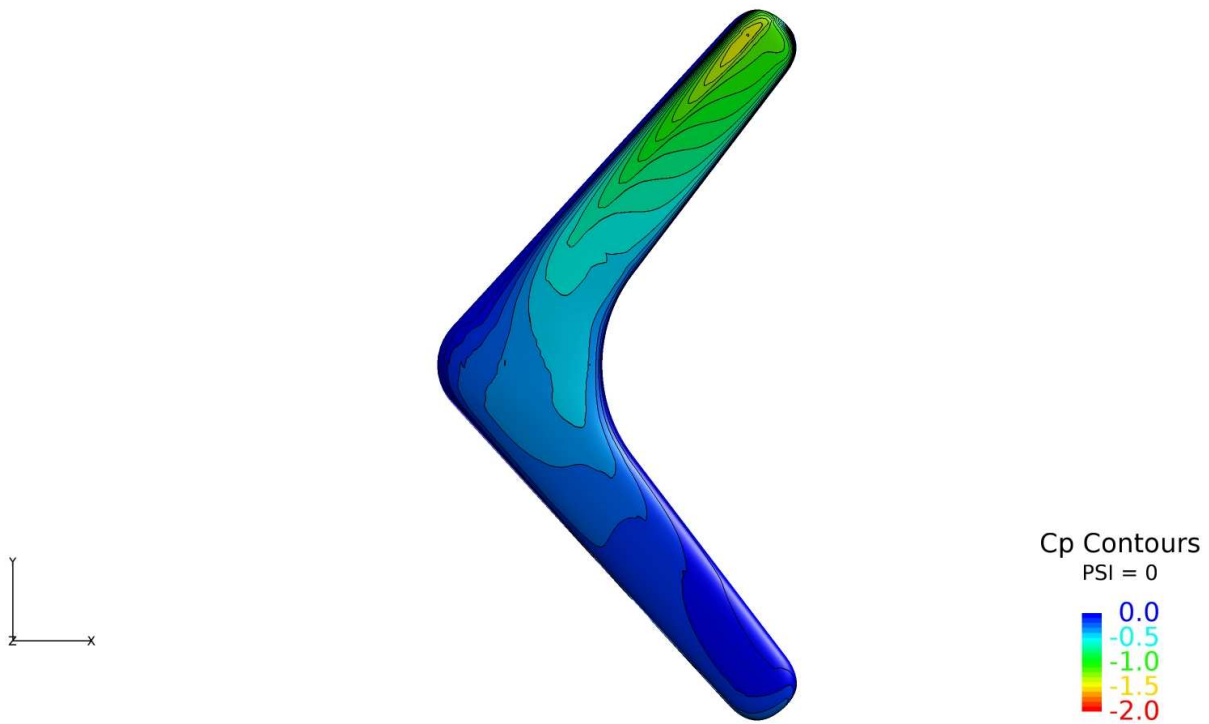


Figure 26. Boomerang Upper-Surface Contours;  $Mach = 0.0774$ ,  $Re = 43,572$ ,  $\chi = 1.0$ ,  $\alpha = 0$ ,  $\psi = 0^\circ$ .

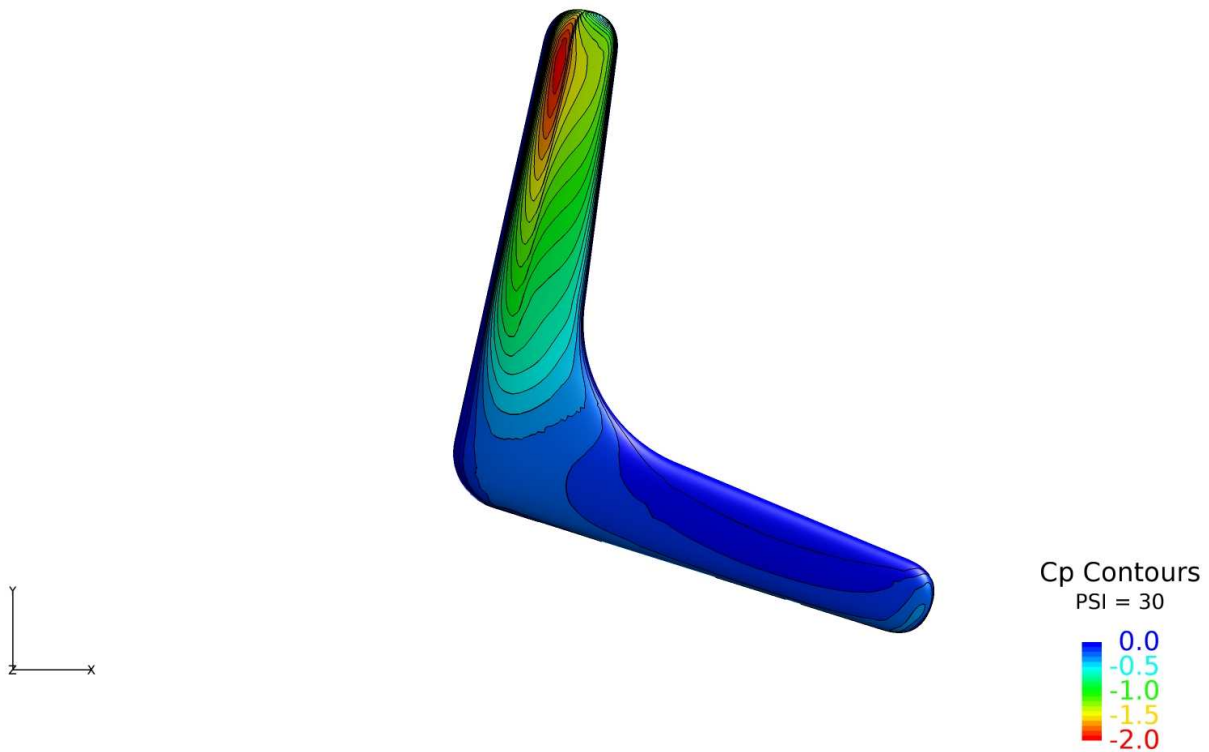


Figure 27. Boomerang Upper-Surface Contours;  $Mach = 0.0774$ ,  $Re = 43,572$ ,  $\chi = 1.0$ ,  $\alpha = 0$ ,  $\psi = 30^\circ$ .

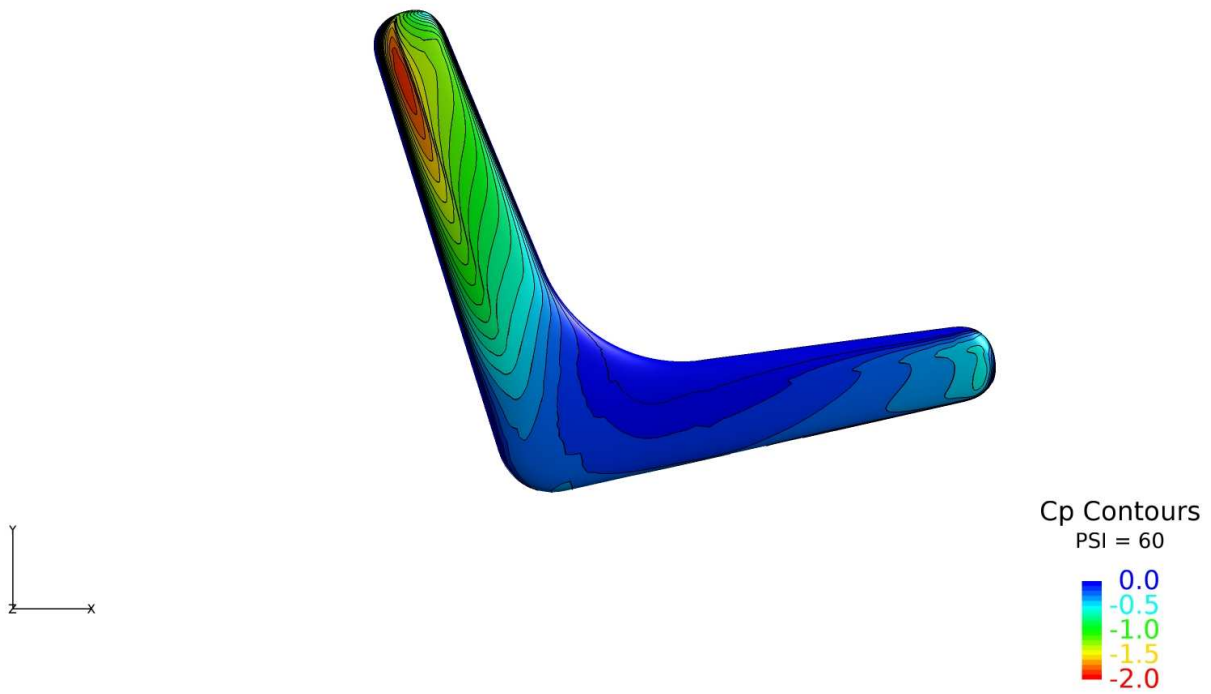


Figure 28. Boomerang Upper-Surface Contours;  $Mach = 0.0774$ ,  $Re = 43,572$ ,  $\chi = 1.0$ ,  $\alpha = 0$ ,  $\psi = 60^\circ$ .

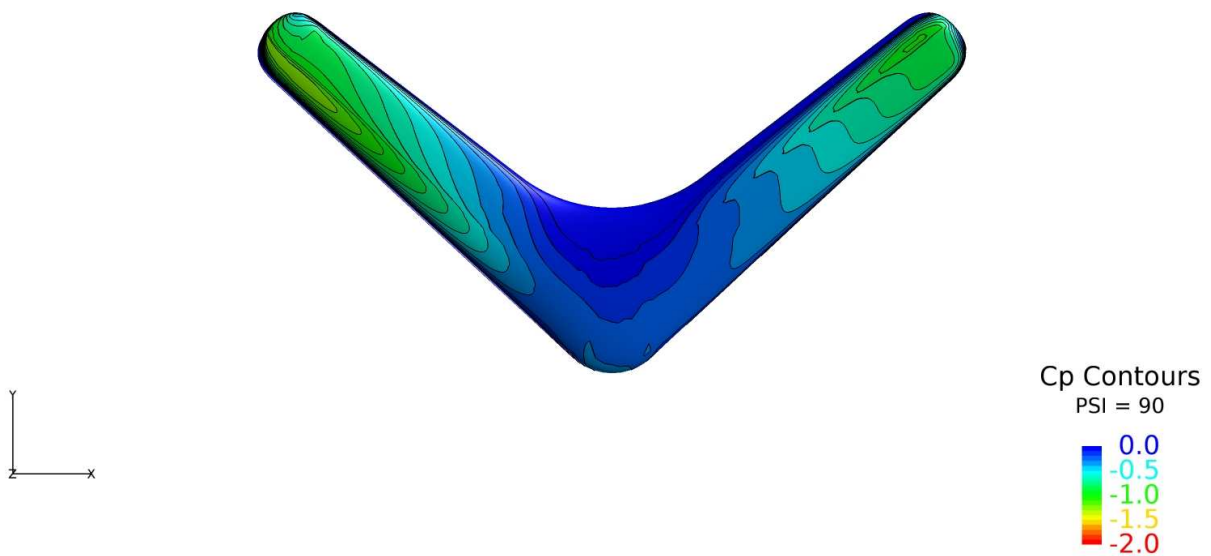


Figure 29. Boomerang Upper-Surface Contours;  $Mach = 0.0774$ ,  $Re = 43,572$ ,  $\chi = 1.0$ ,  $\alpha = 0$ ,  $\psi = 90^\circ$ .

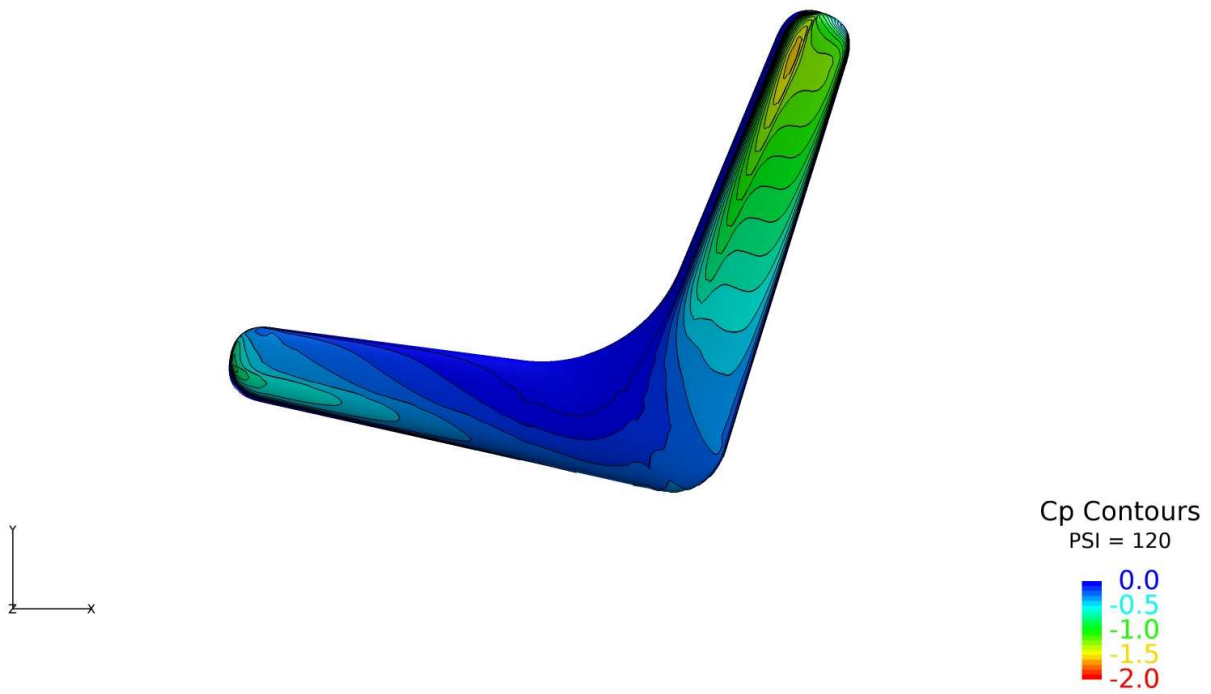


Figure 30. Boomerang Upper-Surface Contours;  $Mach = 0.0774$ ,  $Re = 43,572$ ,  $\chi = 1.0$ ,  $\alpha = 0$ ,  $\psi = 120^\circ$ .

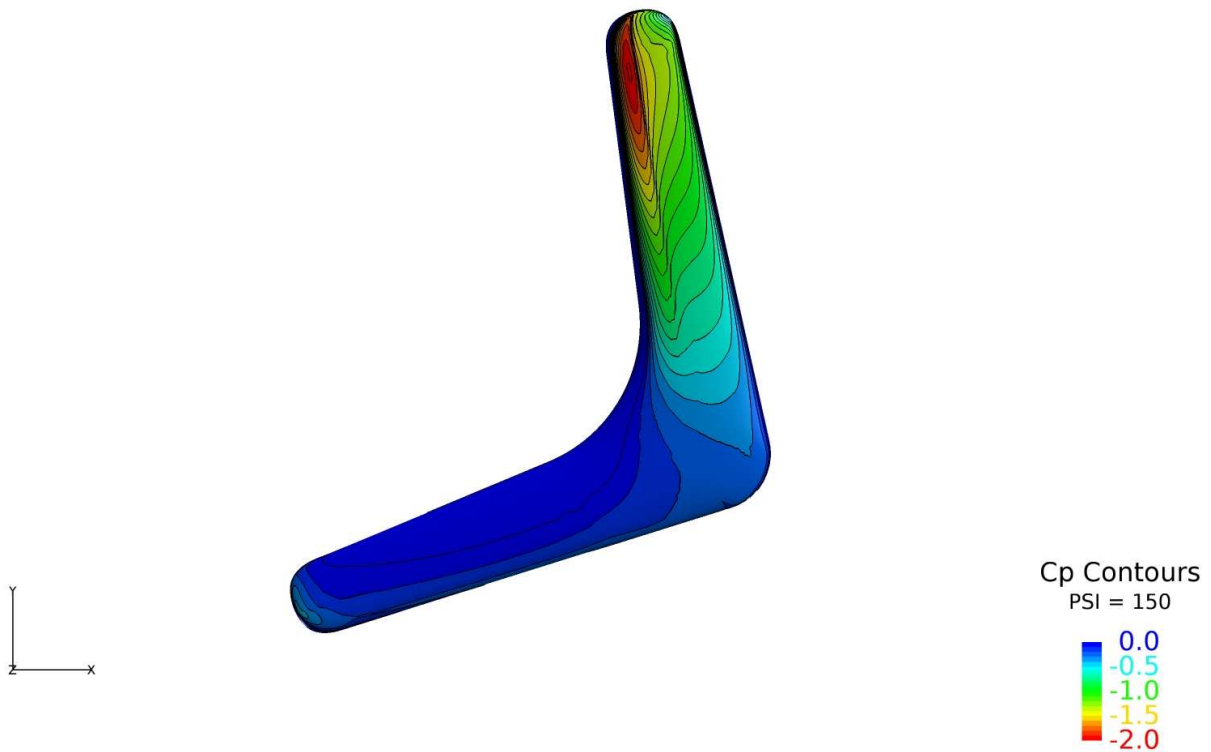


Figure 31. Boomerang Upper-Surface Contours;  $Mach = 0.0774$ ,  $Re = 43,572$ ,  $\chi = 1.0$ ,  $\alpha = 0$ ,  $\psi = 150^\circ$ .

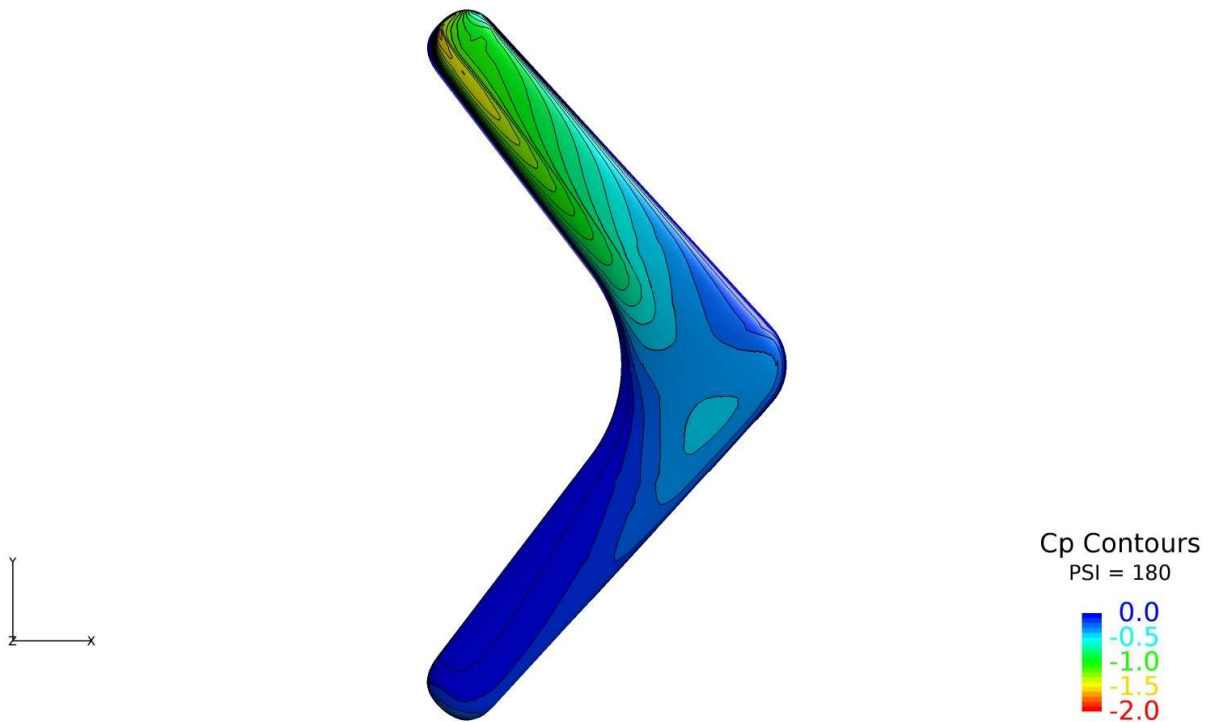


Figure 32. Boomerang Upper-Surface Contours;  $Mach = 0.0774$ ,  $Re = 43,572$ ,  $\chi = 1.0$ ,  $\alpha = 0$ ,  $\psi = 180^\circ$ .

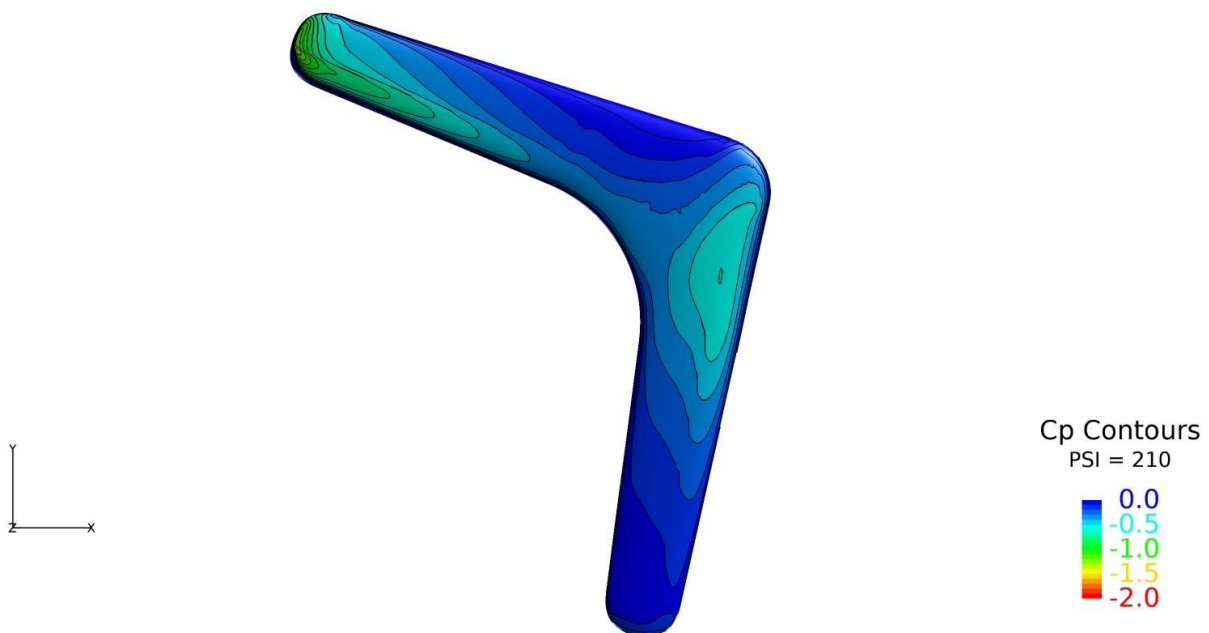


Figure 33. Boomerang Upper-Surface Contours;  $Mach = 0.0774$ ,  $Re = 43,572$ ,  $\chi = 1.0$ ,  $\alpha = 0$ ,  $\psi = 210^\circ$ .

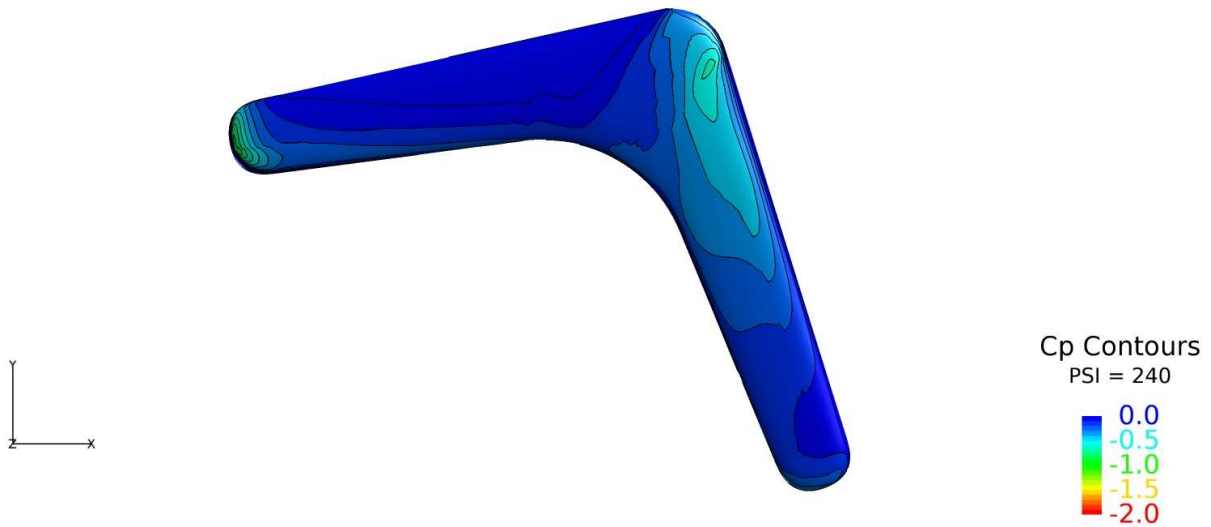


Figure 34. Boomerang Upper-Surface Contours;  $Mach = 0.0774$ ,  $Re = 43,572$ ,  $\chi = 1.0$ ,  $\alpha = 0$ ,  $\psi = 240^\circ$ .

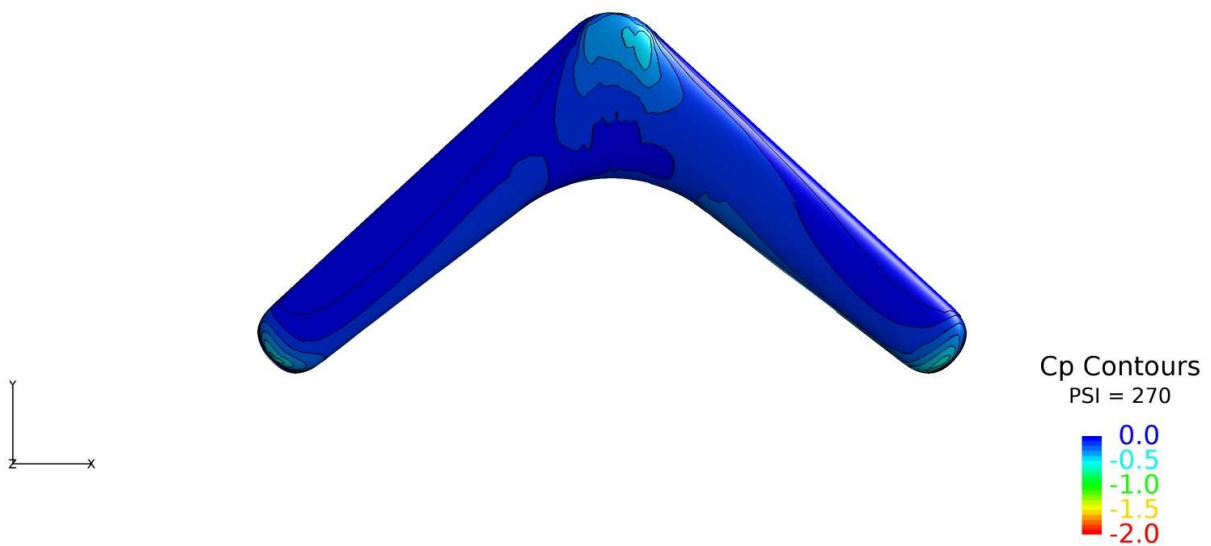


Figure 35. Boomerang Upper-Surface Contours;  $Mach = 0.0774$ ,  $Re = 43,572$ ,  $\chi = 1.0$ ,  $\alpha = 0$ ,  $\psi = 270^\circ$ .



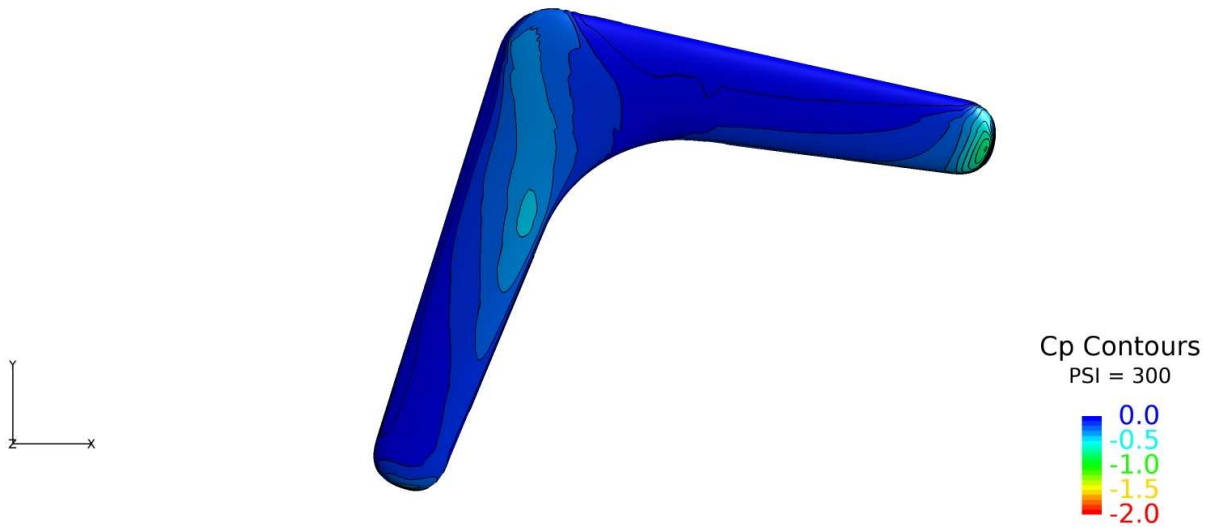


Figure 36. Boomerang Upper-Surface Contours;  $Mach = 0.0774$ ,  $Re = 43,572$ ,  $\chi = 1.0$ ,  $\alpha = 0$ ,  $\psi = 300^\circ$ .

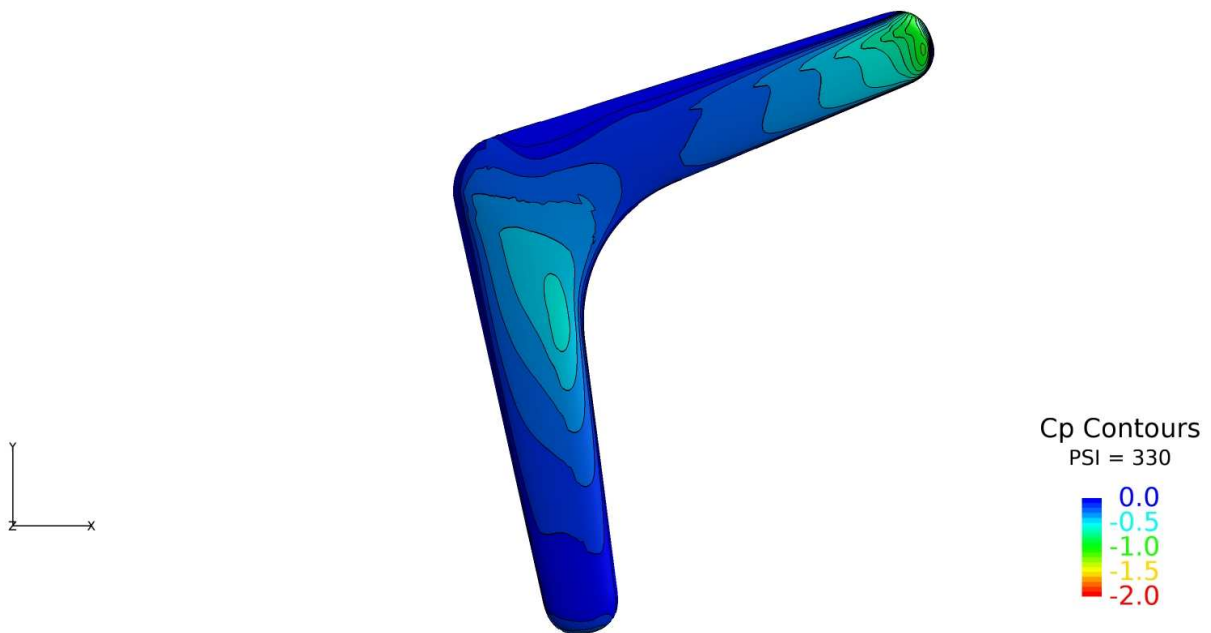


Figure 37. Boomerang Upper-Surface Contours;  $Mach = 0.0774$ ,  $Re = 43,572$ ,  $\chi = 1.0$ ,  $\alpha = 0$ ,  $\psi = 330^\circ$ .

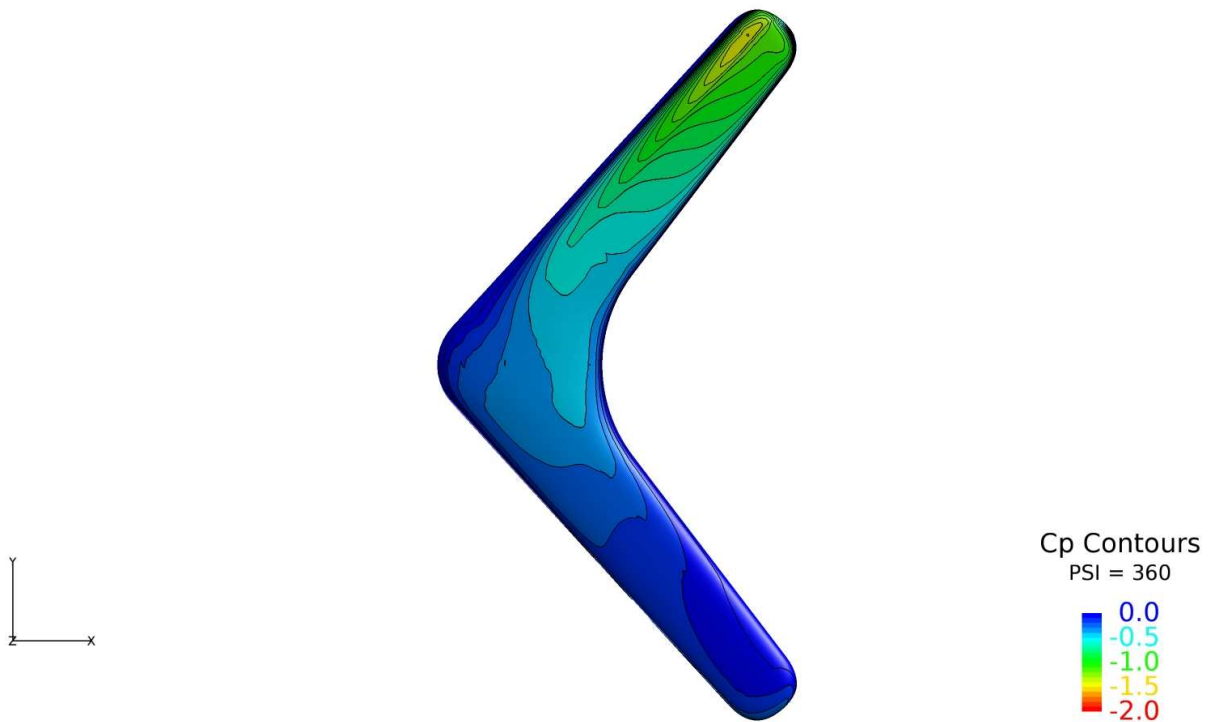


Figure 38. Boomerang Upper-Surface Contours;  $Mach = 0.0774$ ,  $Re = 43,572$ ,  $\chi = 1.0$ ,  $\alpha = 0$ ,  $\psi = 360^\circ$ .

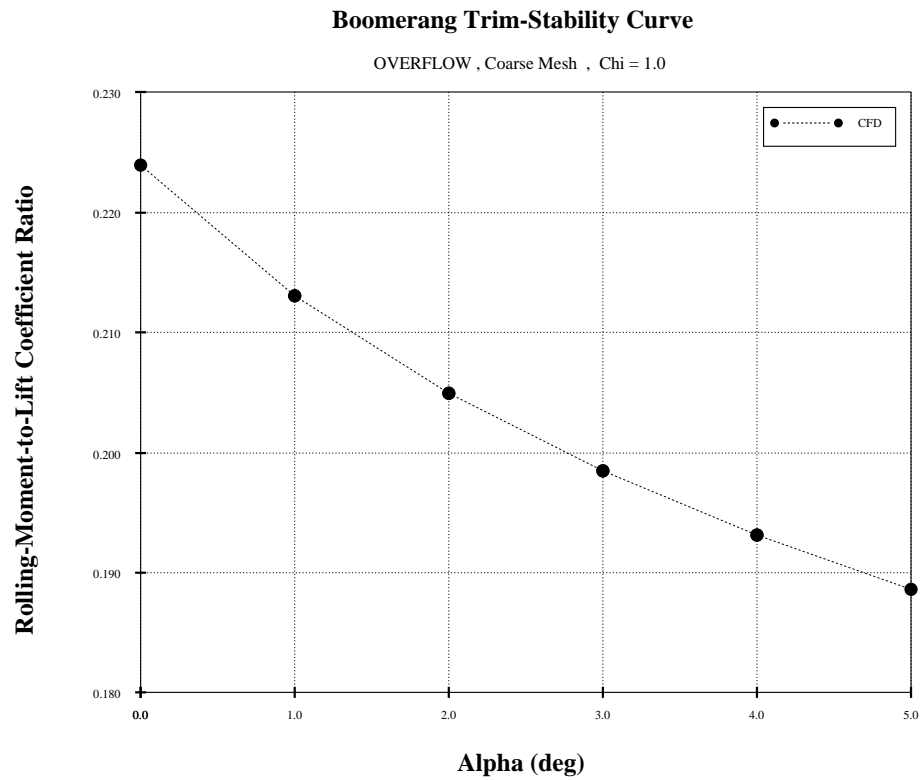


Figure 39. Boomerang Trim-Stability Curve;  $Mach = 0.0774$ ,  $Re = 43,572$ ,  $\chi = 1.0$ , Coarse Mesh.

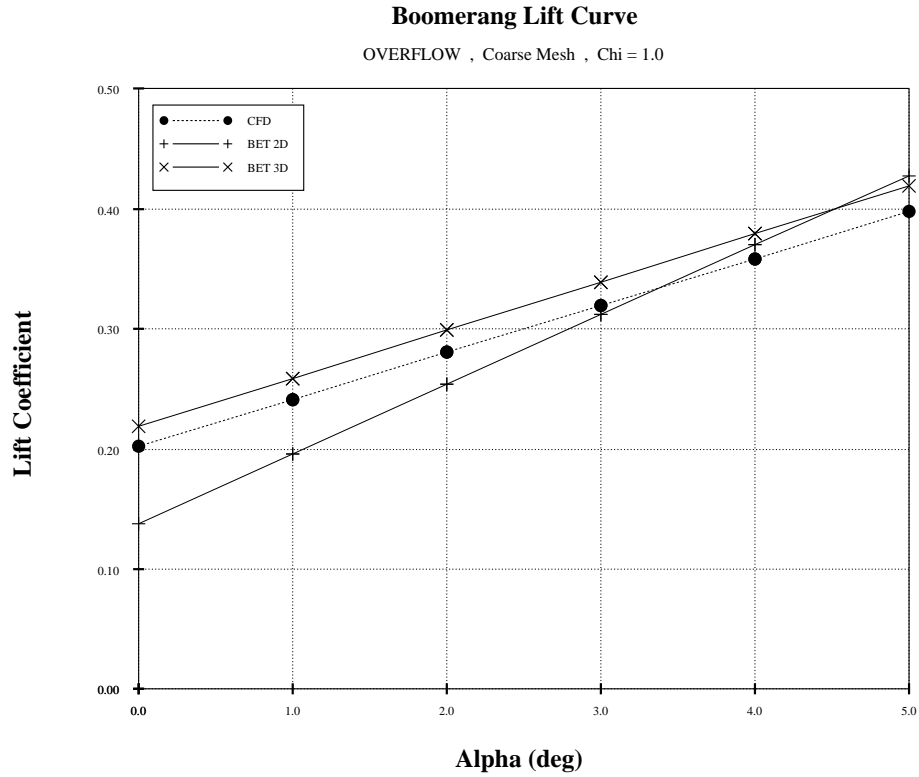


Figure 40. Boomerang Time-Averaged Lift Curve;  $Mach = 0.0774$ ,  $Re = 43,572$ ,  $\chi = 1.0$ , Coarse Mesh.

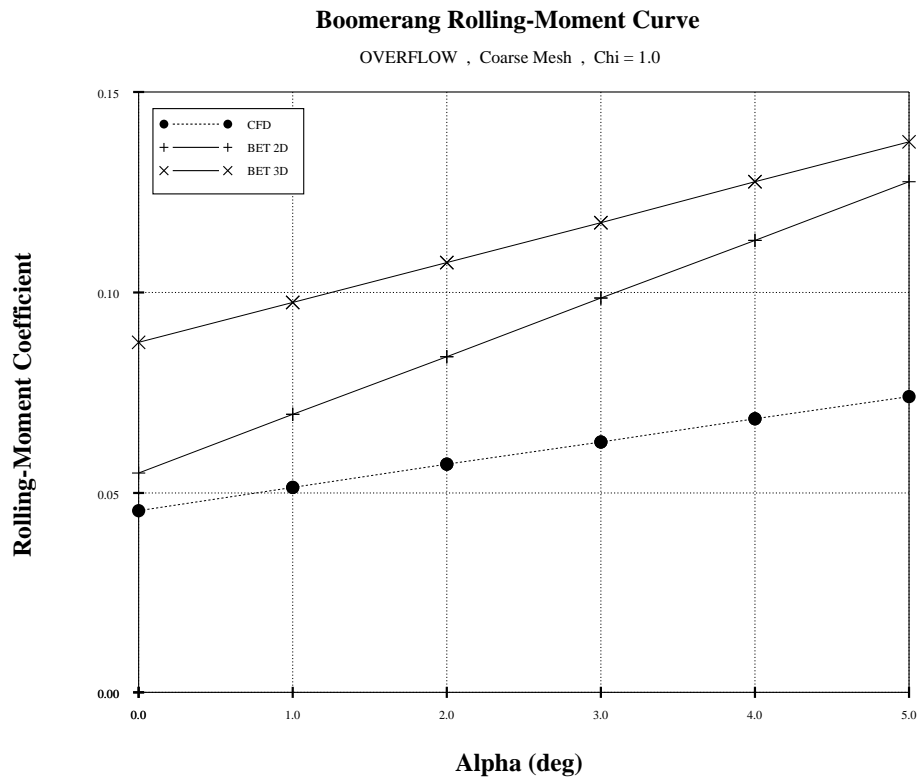
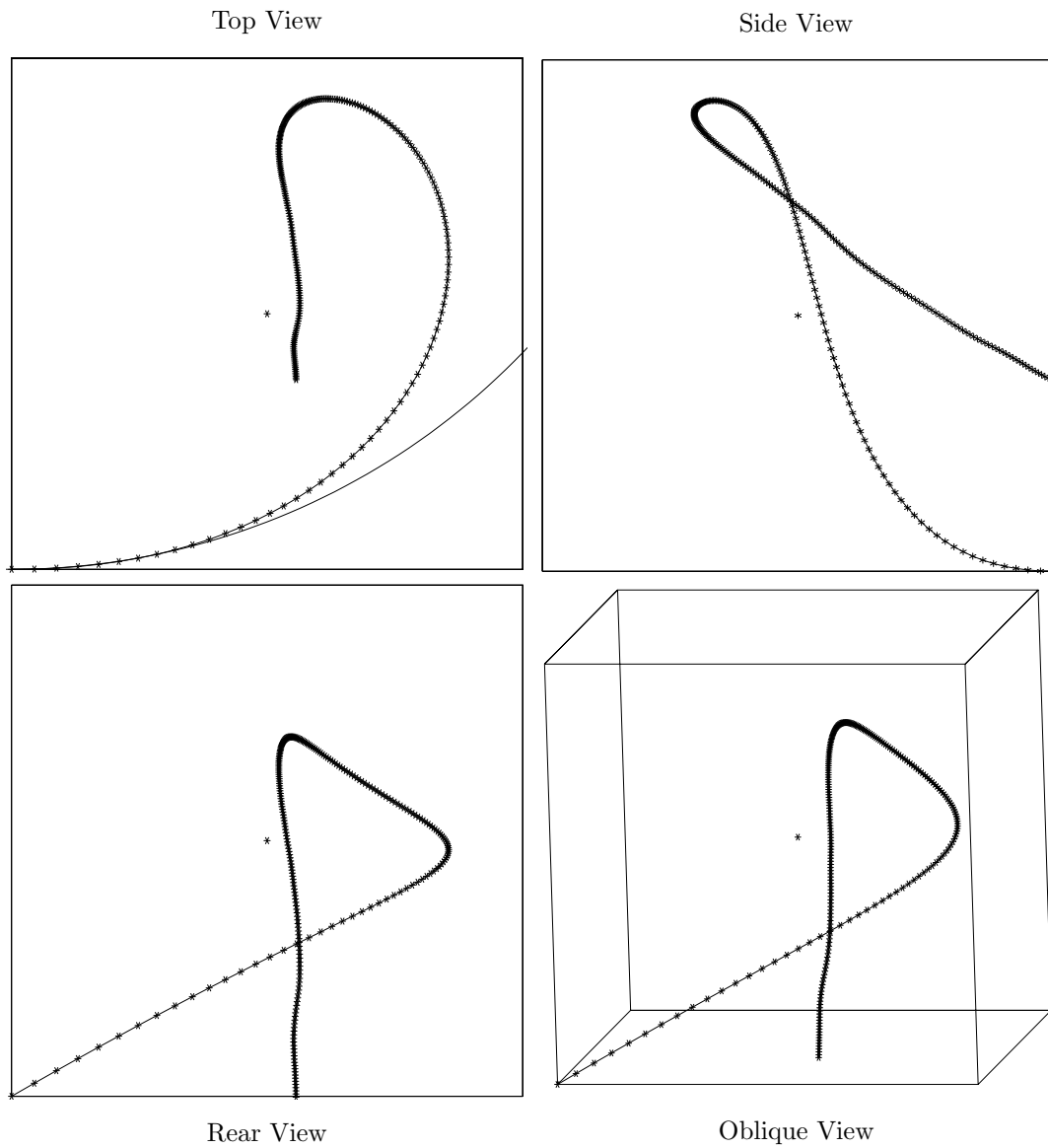
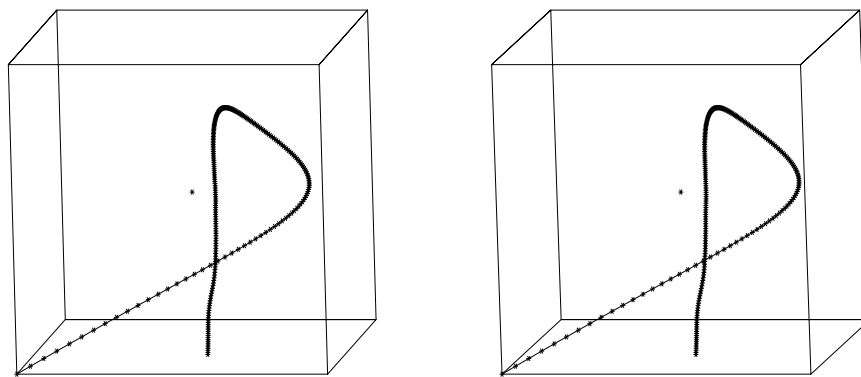


Figure 41. Boomerang Time-Averaged Rolling-Moment Curve;  $Mach = 0.0774$ ,  $Re = 43,572$ ,  $\chi = 1.0$ , Coarse Mesh.



**Figure 42. Preliminary Boomerang Flight Path in a 2,000-inch Box;  $V_0 = 60 \text{ mph}$ ,  $\chi = 1.0$ , Coarse Mesh.**



**Figure 43. Stereoscopic-View of Preliminary Boomerang Flight Path.**